Mechanical Systems and Signal Processing 211 (2024) 111267

Contents lists available at ScienceDirect

Mechanical Systems and Signal Processing

journal homepage: www.elsevier.com/locate/ymssp

AI-driven blind source separation for fast operational modal analysis of structures

Israel Alejandro Hernández-González [a], Enrique García-Macías [a,*], Gabriele Costante [b], Filippo Ubertini [c]

[a] Department of Structural Mechanics and Hydraulic Engineering, University of Granada, Campus de Fuentenueva s/n, 18071 Granada, Spain
[b] Department of Engineering, University of Perugia, Via G. Duranti, 93 - 06125 Perugia, Italy
[c] Department of Civil and Environmental Engineering, University of Perugia, Via G. Duranti, 93 - 06125 Perugia, Italy

ARTICLE INFO

Communicated by D. Bernal

Keywords:
Artificial intelligence
Blind source identification
Damage identification
Deep Neural Networks
Operational Modal Analysis
Structural Health Monitoring

ABSTRACT

The management of the aging built infrastructure stands as a paramount concern on the political agendas worldwide, bearing far-reaching socio-economic impacts. The growing trend of tragic collapses in recent years underscore the urgent need for efficient structural health maintenance (SHM) strategies to support decision-making in prioritizing intervention and rehabilitation actions. Vibration-based SHM systems utilizing Operational Modal Analysis (OMA) have gained popularity owing to their non-destructive nature, global damage assessment capabilities, and relatively straightforward automation with minimal intrusiveness. Nevertheless, state-of-the-art OMA techniques often face significant scalability limitations, primarily driven by extensive computational requirements and need for substantial expert involvement. In this context, recent advances in the realm of artificial intelligence (AI) offer great promise in addressing these scalability issues, paving the way for next-generation SHM systems. In this light, this work introduces a novel Multitask Learning Deep Neural Network (MTL-DNN) model designed for fast and automated blind source modal identification of structures. By encapsulating the principles of second-order blind source identification (SOBI) within the network's architecture, the proposed model can extract the complex-valued modal components concealed within input raw response acceleration data. This enables the direct extraction of complex-valued mode shapes from the weights of the network, and the corresponding resonant frequencies and damping ratios are estimated through a computationally light single-degree-of-freedom identification algorithm. The efficacy of the presented approach is validated through three case studies: a theoretical non-proportionally damped system, a laboratory steel frame structure, and a real-world reinforced concrete arch bridge. The presented results demonstrate the capability of the proposed technique to conduct near-instantaneous automated modal identification with minimal expert intervention, holding great potential as a scalable technique for SHM of large infrastructural systems.

1. Introduction

The management of aging infrastructure poses a paramount challenge for most developed countries. A significant portion of the existing infrastructure was constructed in the aftermath of World War II and, consequently, it is approaching or exceeding its lifespan

* Correspondence to: Department of Structural Mechanics and Hydraulic Engineering, University of Granada, Av. Fuentenueva sn, 18002 Granada, Spain.
E-mail addresses: israela42@correo.ugr.es (I.A. Hernández-González), enriquegm@ugr.es (E. García-Macías), gabriele.costante@unipg.it (G. Costante), filippo.ubertini@unipg.it (F. Ubertini).

https://doi.org/10.1016/j.ymssp.2024.111267
Received 7 September 2023; Received in revised form 30 December 2023; Accepted 16 February 2024
Available online 22 February 2024

of 50–100 years. Tragic collapses, such those of the I-35W bridge in 2007 [1] (Minnesota, US — 13 fatalities), the Morandi Bridge in 2018 [2] (Genoa, Italy — 45 fatalities), or the Nanfang'ao Bridge in 2019 (Yilan County, Taiwan — 6 fatalities), starkly underscore the grave risks of inadequate maintenance. In 2019, the German Federal Highway Research Institute (BASt) [3] reported that 12.2% of the almost 40,000 national road bridges were significantly deteriorated. Likewise, the last report from the American Road & Transportation Builders Association (ARTBA) in 2023 [4] highlighted that 36% of all US bridges–over 222,000 spans–require major repairs, including 76,600 bridges needing outright replacement. These circumstances have spurred substantial R&D actions on the realm of Structural Health Monitoring (SHM) as an effective means of preventive maintenance. In this context, vibration-based SHM approaches through Operational Modal Analysis (OMA) have become particularly popular owing to their minimal intrusiveness, fully non-destructive nature, and suitability for long-term SHM [5]. Nonetheless, despite the growing establishment of OMA techniques in engineering practice, their implementation on a regional scale and across numerous structures introduces new challenges that require innovative solutions.

Output-only OMA techniques exploit ambient response acceleration records to extract the modal signatures of a system, namely its natural frequencies, mode shapes, and damping ratios [6,7]. The fundamental premise is that inferring structural damage becomes feasible through tracking permanent variations in its modal parameters, given their dependency on the mass, stiffness, and damping properties of the monitored structure [8,9]. In this light, considerable research efforts have been devoted in the last decades to the development of diverse time-, frequency-, and time–frequency-domain OMA techniques (interested readers may find a comprehensive state-of-the-art review in Refs. [10–12]). Nonetheless, most recent efforts have focused on the development of automated OMA procedures suitable for continuous SHM [13]. In particular, a number of approaches have been proposed in the literature for the automated interpretation of stabilization diagrams obtained through time-domain Stochastic Subspace Identification (SSI), either in its covariance-driven (CoV-SSI) [14] or data-driven (Data-SSI) [15] versions. These include, among others, hierarchical clustering [16], fuzzy clustering [17], Gaussian Mixture Models (GMM) [18], density-based clustering [19], and blind k-means [20]. Such techniques automate the identification of stable modal poles, enabling the tracing of time series of modal signatures through a modal tracking approach. However, adopting them as a standard for SHM of infrastructural systems at a regional scale is hindered by low efficiency. On one hand, these techniques require expert intervention to set the identification parameters and, on the other hand, they exhibit low computational efficiency when dealing with dense sensor networks.

In recent years, blind source separation (BSS) techniques have garnered growing interest as efficient alternatives to SSI algorithms. Originally emerging in the 1990s as powerful signal processing tools for extracting individual audio sources from recordings, BSS approaches are finding extensive applications in Structural Dynamics. The purpose of BSS is to recover independent components (sources) from the observations (mixing), which holds a direct connection with the modal expansion theorem. The sources are, indeed, the modal responses, whereas the mixing matrix embodies the mode shape matrix of the system [21]. A key advantage of BSS over parametric OMA methods lies in its simplicity. In most cases, the modal identification problem in BSS reduces to resolving a linear system of algebraic equations, thus mitigating the need for model order selection (stabilization diagrams) and lessening the dependence on expert intervention [22]. Once identified, the resonant frequencies and damping ratios of the system can be readily extracted from the independent components using simple single-degree-of-freedom (DOF) identification algorithms. Numerous BSS-based modal identification methods have been developed in recent years [23], with the most notable ones including independent component analysis (ICA) [24], second-order blind identification (SOBI) [25], time–frequency BSS [26], and sparse component analysis (SCA) [27]. Many of these techniques have shown proficiency in OMA of large-scale structures. Noteworthy is the contribution by Yang et al. [28] who proposed a ICA-based time–frequency BSS approach for the modal identification of the University of Southern California (USC) hospital building during the Northridge earthquake in 1994, highlighting the lack of Gaussianity and stationarity assumptions in BSS, unlike classical OMA methods. Xu and co-authors [27] applied SCA to successfully conduct OMA of two full-scale in-operation bridges: a 36 m long steel girder bridge and 109 m long cable-stayed footbridge in Exeter, UK. Li et al. [29] explored the use of SOBI to avoid the need for stabilization diagrams in CoV-SSI, showcasing its efficacy in identifying the modal properties of the Longyangxia hydropower dam in China. Despite these successful experiences that highlight the significantly reduced complexity of BSS techniques compared to standard SSI methods, their automated implementation in infrastructural systems with large-scale structures still requires substantial expert intervention and parameter tuning.

Artificial intelligence (AI) has emerged as a pivotal field of development in today's world, with the potential to revolutionize many aspects of industry and society. In civil engineering, although still in its early stages, several studies in the literature have highlighted the enormous potential of AI in addressing a broad spectrum of problems [30]. These encompass various areas such as the resolution of complex differential equations [31], data compressive sensing [32], computer vision-based structural inspection [33], and data anomaly detection [34]. In the domain of SHM, a substantial portion of research has been dedicated to the extraction of efficient damage indicators [35,36]. Among these, it is worth mentioning the work by Giglioni and co-authors [37], who presented a damage detection approach using autoencoders to reconstruct raw acceleration data. Trained on data collected from a healthy database, the residuals between the AI predictions and newly acquired data can be used as damage sensitive features. Rosso and co-authors [38] explored the use of subspace-based features to train supervised multi-layer perceptron (MLP) networks for multiclass damage classification, showing promise for damage localization in a laboratory I-beam. However, there has been limited exploration of deep learning for modal identification of dynamic systems. Among the few reports in the literature, it is worth noting the work by Liu and co-authors [39], who developed a two-level AI algorithm for SSI. The algorithm includes a model order determination neural network (NN), followed by a second modal identification NN. Their approach showcased comparable accuracy to classical SSI in a real-world suspension bridge, achieving remarkable reductions in computational burden. Similarly, Shim et al. [40] presented an SSI-based long-short term memory (SSI-LSTM) method to track variations in the modal parameters of structures. The developed AI model takes raw acceleration data as input and is trained to reproduce the modal estimates obtained by CoV-SSI, enabling quasi

real-time estimation of the evolution of the modal signatures. While drastically reducing computational demands, the large number of parameters involved in SSI, along with the various user-defined hyper-parameters in the AI, remains a major limitation for extensive implementation. In view of the simplicity of BSS techniques and the potential of AI for developing fast identification models, their combination suggests great potential for addressing the scalability limitations of OMA. This intuition was pursued by Lin et al. [41], who encapsulated the principles of BSS into the loss function of a self-coding NN, yielding promising results in a real-world steel box-girder cable-stayed bridge. Similarly, Shu and co-authors [42] recently developed a multi-task DNN for the automated identification of independent modes extracted from SCA. In this approach, mode shapes are directly extracted as the weights between the last two layers of neurons in the NN, and resonant frequencies and damping ratios are estimated from the independent components using the random decrement technique (RDT). The presented numerical results demonstrated the effectiveness of the NN in a cable-stayed bridge, the Tianjin Yonghe Bridge in Tianjin (China), achieving comparable accuracy levels to FDD and CoV-SSI with critically lower computational time demands.

Motivated by the vast potential of AI for developing next-generation OMA methods, this work presents a novel Multitask Learning Deep Neural Network (MTL-DNN) for fast BSS and automated modal identification of structures. Unlike the previous similar AI approaches reported in the literature (e.g. [41,42]), the present approach employs a multi-task learning deep NN capable of extracting both the real and imaginary components of the independent modal sources, offering comprehensive modal identification capabilities. The developed AI-based OMA approach takes ambient acceleration data as input and provides quasi real-time identification with minimal computational demands. Likewise Ref. [42], the mode shapes (here in complex form) are extracted from the weights between the last two layers of the NN. Subsequently, the resonant frequencies and damping ratios are estimated from the (complex) independent modal components through the robust Ibrahim time-domain (ITD) identification method. Moreover, a set of hard-criteria (HC) are introduced to automatically eliminate the influence of spurious modes (including modal complexity), enabling its applicability for long-term SHM. The effectiveness of the developed approach is appraised through three case studies, involving a (i) theoretical 5-DOFs dynamic system, a (ii) laboratory steel frame, and a (iii) real-world in-operation bridge: the Montecastelli bridge in Italy. The reported results and discussion demonstrate the ability of the proposed approach to conduct fast and automated modal identification with minimal expert intervention, as well as exceptional generalization capabilities for damage identification, showing great promise for extensive SHM of infrastructural systems.

The paper is organized as follows. Section 2 overviews the fundamentals of BSS and the proposed MTL-DNN. Section 3 presents the numerical results and discussion obtained for three different case studies, namely (i) a theoretical 5-degree-of-freedom system, (ii) and laboratory steel frame, and (iii) a real-world in-operation bridge, the Montecastelli Bridge in Italy. Finally Section 4 closes the manuscript with some concluding remarks.

2. Theoretical background

2.1. Second order blind identification

The governing equation of motion of an n-degree-of-freedom (DOF) dynamic system can be expressed according to the principles of structural dynamics theory as:

$$\mathbf{M}\ddot{\mathbf{X}}(t) + \mathbf{C}\dot{\mathbf{X}}(t) + \mathbf{K}\mathbf{X}(t) = \mathbf{F}(t), \tag{1}$$

with $\mathbf{M}$, $\mathbf{C}$ and $\mathbf{K} \in \mathbb{R}^{n\times n}$ denoting the mass, damping, and stiffness matrices of the system. The vectors $\mathbf{F}(t)$ and $\mathbf{X}(t) \in \mathbb{R}^n$ are the external force and the response displacement vectors, respectively, and dot notation is used to indicate differentiation with respect to time. Let us consider that only a number $m \in \mathbb{N}^*$ of sensors are available, recording a measurement data vector $\mathbf{x}(t) \in \mathbb{R}^m$. Assuming the system is linear time-invariant and a number $l \in \mathbb{N}^*$ of natural modes of vibration are excited, the system's response can be expanded using modal superposition as:

$$\mathbf{x}(t) = \boldsymbol{\Phi}\,\mathbf{q}(t) = \sum_{i=1}^{l} \boldsymbol{\varphi}_i q_i(t), \tag{2}$$

where $\boldsymbol{\Phi} \in \mathbb{C}^{m\times l}$ is the modal matrix composed of l mode shape vectors $\boldsymbol{\varphi}_i \in \mathbb{C}^m$, and $\mathbf{q}(t) = \left[q_1(t), \ldots, q_l(t)\right]^{\mathrm{T}}$ stands for the modal displacement vector. Note that, in general, the modal matrix is complex-valued when the damping matrix $\mathbf{C}$ is non-classical. In large-scale civil engineering structures, complex mode shapes can arise for various reasons [43], including the existence of non-proportional and non-viscous damping, gyroscopic effects, asynchronous sampling, non-linearities, or limitations in the identification of low-excited modes.

In this context, the dynamic identification problem reduces to the estimation of the modal responses $\mathbf{q}(t)$ and mode shapes $\boldsymbol{\Phi}$ from the system response $\mathbf{x}(t)$. In particular, BSS techniques seek a set of signals $\mathbf{s}(t)$, the so-called sources or independent components, from observations of their mixtures in $\mathbf{x}(t)$ [44]:

$$\mathbf{x}(t) = \mathbf{A}\mathbf{s}(t) + \mathbf{n}(t), \tag{3}$$

where $\mathbf{A} \in \mathbb{C}^{m\times n}$ is the so-called mixing matrix, and $\mathbf{n}(t)$ represents an additive (temporally and spatially) stationary white noise. Upon comparing Eqs. (2) and (3), it becomes apparent that the mixing-matrix and the independent components are related to the modal matrix and the modal displacements, respectively. Among the various BSS techniques available in the literature (refer to Ref. [23] for a comprehensive state-of-the-art review), second-order blind identification (SOBI) has been adopted in this work due to its

demonstrated potential for conducting OMA and its robustness against measurement noise [45]. A fundamental assumption in SOBI is that the sources are stationary and shift-uncorrelated, so their covariance matrix at a time lag τ reads [46]:

$$\mathbf{R}_s(\tau) = \mathbb{E}\left[\mathbf{s}(t)\mathbf{s}^{\mathrm{H}}(t+\tau)\right] = \mathrm{diag}\left[\varrho_1, \ldots, \varrho_n\right], \tag{4}$$

where superscript "H" denotes the complex conjugate transpose operator. In addition, the sources are often scaled to have unit variance, i.e. $\mathbf{R}_s(0) = \mathbf{I}$. Therefore, from Eq. (3), the correlation matrix of the observations can be stated as:

$$\mathbf{R}_x(\tau) = \mathbb{E}\left[\mathbf{x}(t)\mathbf{x}^{\mathrm{T}}(t+\tau)\right] = \mathbf{A}\mathbf{R}_s(\tau)\mathbf{A}^{\mathrm{H}}, \tag{5}$$

which, given that $\mathbf{R}_s(\tau)$ is a diagonal matrix, reveals that the mixing matrix $\mathbf{A}$ can be identified through a diagonalization procedure. It is important to emphasize that the mixing model in Eq. (3) is the sole model assumption in BSS. Therefore, BSS techniques may be used as a time-domain non-parametric modal identification approach in the presence of some types of non-linearities.

In general, the diagonalization problem in Eq. (5) is overdetermined, with the rank of $\mathbf{A}$ being $n \leq m$. For simplicity, and given that determined SOBI suffices for the investigated case studies in Section 3, the complex-valued extension reported by McNeill [47] of the determined SOBI algorithm in [25] has been adopted in this work. Nevertheless, to solve the under-determined problem, that is the case in which there are more hidden components n than sensors m, different approaches are available in the literature, including (i) the application of SOBI to different frequency broadbands containing $\leq m$ components, (ii) combining BSS with concepts from state–space control theory [48], and (iii) adopting simultaneous matrix diagonalization-based techniques [49].

The SOBI algorithm proposed by McNeill [47] allows the identification of complex-valued mixing matrices $\mathbf{A}$ (and so, complex mode shapes) by augmenting the recorded signals $\mathbf{x}(t)$ in their analytic form through the Hilbert transform. The Hilbert transform of $\mathbf{x}(t)$, $\tilde{\mathbf{x}}(t) = \mathcal{H}(\mathbf{x}(t))$, imparts a phase shift of 90 degrees, that is $\mathscr{F}(\tilde{\mathbf{x}}(t))(\omega) = -i\mathrm{sgn}\,\mathscr{F}(\mathbf{x}(t))$ [50], $\mathscr{F}$ and $i = \sqrt{-1}$ denoting the Fourier transform operator and the imaginary unit, respectively. If adopting the augmented measured data, $\check{\mathbf{x}}(t) = \mathbf{x}(t) + i\,\tilde{\mathbf{x}}(t)$, the mixing model in Eq. (3) can be simply reformulated as $\check{\mathbf{x}}(t) = \mathbf{A}\check{\mathbf{s}}(t)$ [25].

Then, the core step in the SOBI algorithm involves estimating an orthogonal matrix $\boldsymbol{\Psi}$ that approximately diagonalizes several time-shifted covariance matrices with time lags τ_i, $1 \leqslant i \leqslant p$. Following the original SOBI algorithm reported in [25], this is accomplished using the joint approximate diagonalization (JAD) algorithm proposed by Belouchrani et al. [51]. This JAD algorithm, based on the Jacobi rotation technique, is well-suited for joint diagonalizing unitary matrices (i.e. $\mathbf{A}^{\mathrm{H}}\mathbf{A} = \mathbf{A}\mathbf{A}^{\mathrm{H}} = \mathbf{I}$); therefore, it is necessary to first whiten the observed data. Whitening or sphering consists of a linear transformation to $\check{\mathbf{x}}(t)$ such that the whitened data $\mathbf{z}(t)$ are uncorrelated and have unit variance. This can be accomplished by removing the mean from $\check{\mathbf{x}}$ and normalizing its covariance matrix using principal component analysis (PCA). The latter is carried out through the eigenvalue decomposition of the covariance matrix of the observations, that is $\mathbb{E}\left\{\check{\mathbf{x}}(t)\check{\mathbf{x}}(t)^{\mathrm{H}}\right\} = \mathbf{R}_x(0) = \mathbf{E}\mathbf{D}\mathbf{E}^{\mathrm{H}}$, where $\mathbf{D}$ and $\mathbf{E}$ correspond to the diagonal eigenvalue and the orthogonal eigenvector matrices, respectively. On this basis, the whitened (zero-mean, unit variance; $\mathbf{R}_z(0) = \mathbf{I}$) data vector $\mathbf{z}(t)$ can be obtained as:

$$\mathbf{z}(t) = \mathbf{D}^{-1/2}\mathbf{E}^{\mathrm{H}}\check{\mathbf{x}}(t) = \mathbf{W}_{\mathrm{m}}\check{\mathbf{x}}(t) = \mathbf{A}'\,\check{\mathbf{s}}(t), \tag{6}$$

where matrix $\mathbf{W}_{\mathrm{m}} = \mathbf{D}^{-1/2}\mathbf{E}^{\mathrm{H}}$ is the so-called whitening matrix. It is important to note that the effect of whitening is to transform the mixing matrix $\mathbf{A}$ into a new unitary mixing matrix $\mathbf{A}' = \mathbf{W}_{\mathrm{m}}\mathbf{A}$, so that the whitened data $\mathbf{z}(t)$ can be used for unitary JAD. The JAD algorithm aims to minimize the off diagonal terms of $\boldsymbol{\Psi}^T\mathbf{R}_z(\tau_i)\boldsymbol{\Psi}$ for p covariance matrices, which can be formalized through the following optimization problem [25]:

$$\boldsymbol{\Psi}^{\mathrm{H}}\mathbf{R}_z(\tau_i)\boldsymbol{\Psi} \approx \mathrm{diag}\left[\rho_1(\tau), \ldots, \rho_m(\tau)\right] \Rightarrow \min_{\boldsymbol{\Psi}} \sum_{i=1}^{p} \mathrm{off}\left(\boldsymbol{\Psi}^{\mathrm{H}}\mathbf{R}_z(\tau_i)\boldsymbol{\Psi}\right), 1 \leq i \leq p, \tag{7}$$

where $\mathbf{R}_z(\tau) = \mathbb{E}\left\{\mathbf{z}(t)\mathbf{z}(t+\tau)^{\mathrm{H}}\right\}$ is the time-shifted covariance matrix of the whitened data, and terms $\rho_i(\tau)$ denote their autocovariances. Thus, the mixing matrix $\mathbf{A}$ and the independent components $\check{\mathbf{s}}$ can be obtained as [52]:

$$\mathbf{A} = \mathbf{W}_{\mathrm{m}}^{-1}\boldsymbol{\Psi} = \mathbf{E}\mathbf{D}^{1/2}\boldsymbol{\Psi}, \text{ and } \check{\mathbf{s}} = \mathbf{W}\check{\mathbf{x}}, \tag{8}$$

with $\mathbf{W} = \mathbf{A}^{-1}$ denoting the de-mixing matrix. Once extracted, the mode shapes (arbitrarily scaled in the case of OMA) are directly extracted from the mixing matrix $\mathbf{A}$. On the other hand, the resonant frequencies and damping ratios can be readily derived from the independent components $\check{\mathbf{s}}(t)$ using a single-degree-of-freedom (SDOF) modal identification approach. Note that the real or imaginary parts of $\check{\mathbf{s}}(t)$ have the same power spectral density (PSD) and only differ in phase. There, the identification can be conducted on either of them or, alternatively, the averaged independent components $\bar{\mathbf{s}}(t) = \left[\mathrm{Re}(\check{\mathbf{s}}(t)) + \mathrm{Imag}(\check{\mathbf{s}}(t))\right]/\sqrt{2}$ [25] (the $1/\sqrt{2}$ factor is introduced to preserve the PSD amplitude).

The modal identification problem in SOBI relies on the evidence that the modal displacements in Eq. (2) are approximately shift-uncorrelated [25]. Nevertheless, it is important to note that $\mathbf{q}(t)$ are not perfectly shift-uncorrelated (mutually independent), which may induce certain errors in the modal identification estimates by SOBI. The presence of some time correlation among the modal displacements stems from the inherent characteristics dynamic systems, which are generally damped (non-conservative), and the finite length of the observation data (refer to Ref. [53] for a further theoretical discussion). While the first limiting factor is typically unavoidable in practice, SOBI has demonstrated proficiency in separating lightly damped modes [54], as it is often the case in most civil engineering structures. Instead, modal correlation effects induced by discrete sampling can be effectively minimized

by windowing the input data before applying SOBI. In this work, as recommended by McNeill and Zimmerman [25], a Gaussian window has been adopted, which is given by:

$$w(\hat{t}) = e^{-0.5(\alpha\hat{t})^2},\ \hat{t} = \frac{2}{t_{max}}t - 1, \tag{9}$$

where $\hat{t} \in [-1, 1]$ denotes a normalized time, t_{max} is the time duration of the data, and α is the spectral bandwidth parameter of the window. In this work, the bandwidth parameter has been set to $\alpha = 2.5$, a value within the recommended range in [25], after inspecting the correlation functions obtained in the different case studies presented hereafter. Other alternative one-step JAD algorithms are available in the literature requiring no pre-whitening, such as the high-performance Weighted Exhaustive Diagonalization with Gauss itErations (WEDGE) [55] or parallel factor (PARAFAC) decomposition [49].

Lastly, it is important to remark that the assumption of approximately time-shift uncorrelated modal displacements holds true only for free vibrations or random white excitations. However, when forcing is colored random in the vicinity of the natural frequencies of the system, the deviation of the excitation forces from a flat spectrum may introduce time correlation between the modal displacements, thus diminishing the quality of the modal estimates by SOBI.

Recall that both the mixing matrix and the independent components are complex-valued, hence one can write:

$$\mathbf{A} = \mathbf{A}_R + i\,\mathbf{A}_C, \quad \mathbf{s} = \mathbf{s}_R + i\,\mathbf{s}_C, \quad \text{with } \mathbf{A}_R, \mathbf{A}_C \in \mathbb{R}^{m\times n},\ \mathbf{s}_R, \mathbf{s}_C \in \mathbb{R}^{n\times 1}, \tag{10}$$

where the "R" and "C" indexes correspond to the real and imaginary parts of the respective terms. Then, substituting Eq. (10) into (3), and considering that the observed data $\mathbf{x}(t)$ are real-valued, it can be readily found that the condition $\mathbf{A}_R\,\mathbf{s}_C + \mathbf{A}_C\,\mathbf{s}_R = \mathbf{0}$ must be satisfied. In this light, the system's response $\mathbf{x}$ can be expressed as a linear combination of the real and imaginary parts of $\mathbf{s}(t)$ as:

$$\mathbf{x}(t) = \left(\mathbf{A}_R + i\,\mathbf{A}_C\right)\left(\mathbf{s}_R(t) + i\,\mathbf{s}_C(t)\right) = \mathbf{A}_R\,\mathbf{s}_R(t) - \mathbf{A}_C\,\mathbf{s}_C(t), \tag{11}$$

and, hence, the system's response can be expressed as the mixing of two independent sources, $s_R(t)$ and $s_C(t)$, each phase-shifted by 90 degrees, and mixed using two separate mixing matrices, $\mathbf{A}_R$ and $\mathbf{A}_C$.

2.2. AI-driven BSS: MTL-DNN

Building upon the formulation of the SOBI algorithm outlined above, a novel multitask learning deep neural network (MTL-DNN) for automated OMA of structures is presented herein. The primary goal of the proposed network is to simultaneously extract the real and imaginary parts of the independent components, so enabling the identification of complex mode shapes.

2.2.1. Network architecture

The fundamental steps in the BSS formulation described above are encapsulated in the architecture of the proposed MTL-DNN. Drawing upon the findings previously reported in Eq. (11), this is achieved by defining two separate branches in the network with the objective of estimating the real and imaginary parts of the independent components $\mathbf{s}(t)$. These two branches are then fully connected through linear activation functions, resulting in the mixing matrix (mode shapes) in complex form. In this light, the architecture of the proposed MTL-DNN is sketched in Fig. 1. The input of the MTL-DNN corresponds to the measured acceleration time series $\mathbf{x}(t)$, discretely acquired with a sampling frequency f_s or, alternatively, with a time step $\Delta t = 1/f_s$. The output of the network is the reconstructed signal $\mathbf{x}'(t)$ produced by the network after applying Eq. (3) with the estimated mixing matrix. To account for the sequential nature of the input time series, a time lag τ is imposed between the observation data $\mathbf{x}(t)$ and the outputs of the network (i.e. $\mathbf{s}(t)$ and $\mathbf{x}'(t)$). This allows the network to capture and learn the temporal correlations between the inputs and the outputs (see Fig. 1).

The number of input neurons is equal to the number of sensors in the structure. This is followed by d dense layers of f neurons per layer ("H"), which simulate the whitening process and the JAD technique of the BSS. The second and the second-to-last layers of this group, as well as the second-to-last layers of branches "J" and "K" introduced hereafter, are regularization (dropout) layers ("D") aimed at favoring the generalization of the network. The working principle of these layers lies in the removal of some neurons, so that their contribution to the activation of downstream neurons is temporally removed on the forward pass, and any weight updates are not applied to the neurons on the backward pass. Therefore, the remaining neurons will have to handle the representation required to make predictions for the missing neurons, allowing the network to learn multiple independent internal representations and becoming less sensitive to the specific weights of neurons, resulting in a network with better generalization and less prone to overfitting the training data. The following part of the network is divided into two dense branches ("J" and "K"), both containing h dense layers with g neurons per layer, except for the last layers of these two branches that contain n neurons, equal to the number of identified independent components. As aforementioned, this division serves the primary purpose of separating the real and complex part of the independent components, as extracted in the output layers $\mathbf{R}$ and $\mathbf{C}$ of branches "K" and "J", respectively. From Eq. (10), it can be obtained that $\mathbf{s}_R = \mathbf{R}$, $\mathbf{s}_C = \mathbf{C}$, and $\mathbf{s} = \mathbf{R} + i\,\mathbf{C}$. Thus, the complex independent components $\mathbf{s}$ for an input time series of N data-points can be extracted from the outputs of layers $\mathbf{R}$ and $\mathbf{C}$ as:

$$\mathbf{s} = \begin{bmatrix} R_{11} + i\,C_{11} & \cdots & R_{1j} + i\,C_{1j} & \cdots & R_{1n} + i\,C_{1n} \\ \vdots & & \vdots & & \vdots \\ R_{i1} + i\,C_{i1} & \cdots & R_{ij} + i\,C_{ij} & \cdots & R_{in} + i\,C_{in} \\ \vdots & & \vdots & & \vdots \\ R_{N1} + i\,C_{N1} & \cdots & R_{Nj} + i\,C_{Nj} & \cdots & R_{Nn} + i\,C_{Nn} \end{bmatrix} \in \mathbb{C}^{N\times n}. \tag{12}$$

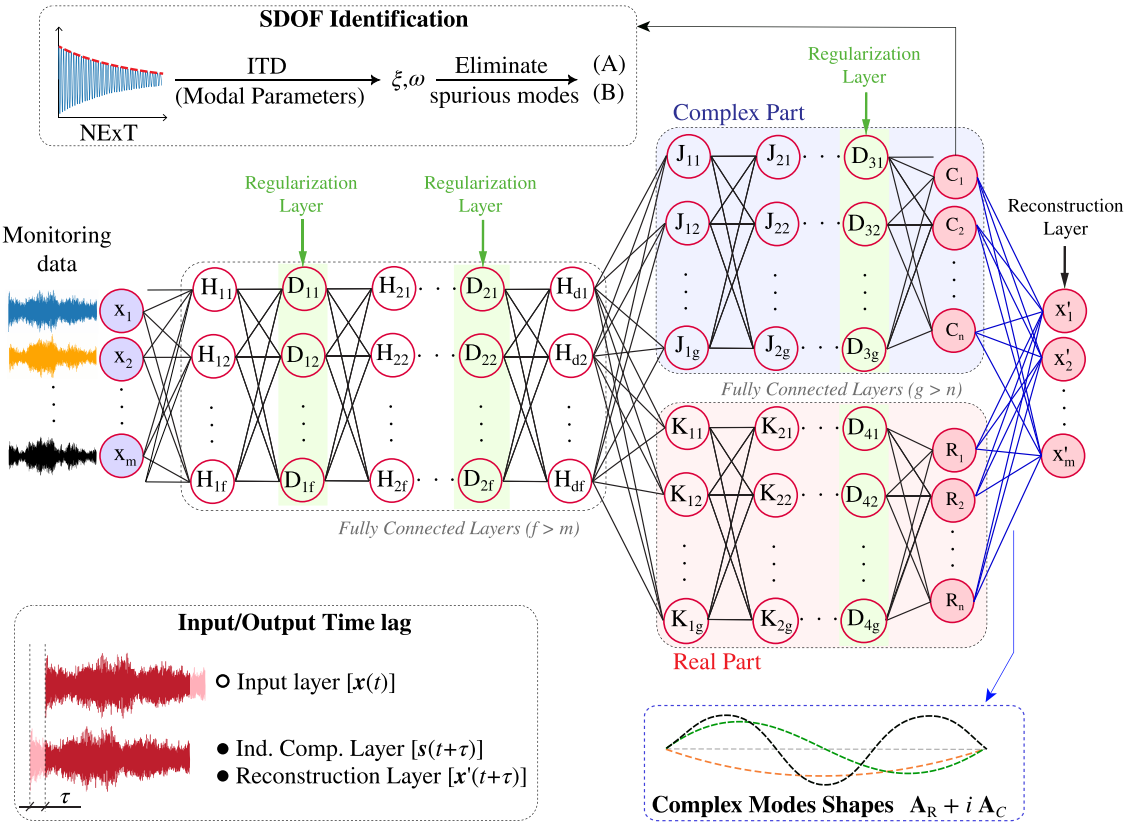

Fig. 1. Architecture of the proposed MTL-DNN for automated operational modal analysis of structures.

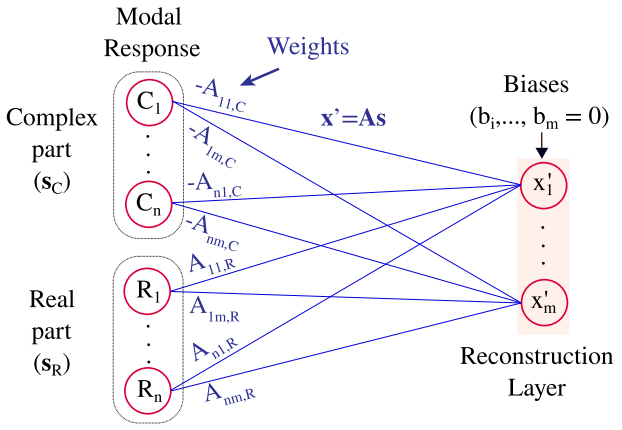

Fig. 2. Weights between the penultimate and final layers of the MTL-DNN used for the estimation of complex mode shapes.

Fig. 2 shows a detailed view of the penultimate and last layers of the neural network. The last layer has as a linear activation function so that the outputs of the network x'_j (considering the biases equal to 0) have the expression:

$$x'_j = \sum_{r=1}^{n} \left[(R_r A_{rj,R}) - (C_r A_{rj,G}) \right], \quad \mathbf{A}_R = \begin{bmatrix} A_{11,R} & \cdots & A_{n1,R} \\ \vdots & \ddots & \vdots \\ A_{1m,R} & \cdots & A_{nm,R} \end{bmatrix}, \quad \mathbf{A}_C = \begin{bmatrix} A_{11,C} & \cdots & A_{n1,C} \\ \vdots & \ddots & \vdots \\ A_{1m,C} & \cdots & A_{nm,C} \end{bmatrix}. \tag{13}$$

Note that the weights between layers **R** and **C** and the reconstruction layer represent the real and imaginary parts of the mode shapes ($\mathbf{A}_R$, and $\mathbf{A}_C$) as shown in Eq. (13). Comparing Eqs. (10) and (13), the mixing matrix containing the complex mode shapes

can be obtained as:

$$\mathbf{A}=\begin{bmatrix} A_{11,R}+i\ A_{11,C} & \dots & A_{i1,R}+i\ A_{i1,C} & \dots & A_{n1,R}+i\ A_{n1,C} \\ \vdots & & \vdots & & \vdots \\ A_{ij,R}+i\ A_{ij,C} & \dots & A_{ij,R}+i\ A_{ij,C} & \dots & A_{ij,R}+i\ A_{ij,C} \\ \vdots & & \vdots & & \vdots \\ A_{1m,R}+i\ A_{1m,C} & \dots & A_{im,R}+i\ A_{im,C} & \dots & A_{nm,R}+i\ A_{nm,C} \end{bmatrix}\in\mathbb{C}^{m\times n}. \tag{14}$$

Along with the reconstructed signals, the output of the branches **R** and **C** (i.e. $\mathbf{s}_r$ and $\mathbf{s}_c$) are also monitored. In this way, the loss function for the MTL-DNN is defined as:

$$L=\frac{1}{N}\left[\sum_{l=1}^{n}\sum_{i=1}^{N}\left(R_{il,\tau}-\hat{R}_{il}\right)^2+\sum_{l=1}^{n}\sum_{i=1}^{N}\left(C_{il,\tau}-\hat{C}_{il}\right)^2+\sum_{l=1}^{m}\sum_{i=1}^{N}\left(x_{il,\tau}-\hat{x}_{il}\right)^2\right]+w_d\mathrm{L2}_{norm}(\text{weights}), \tag{15}$$

where $R_{il,\tau}$ and $C_{il,\tau}$ represent the real and complex part of the modal response obtained by SOBI, respectively; $\hat{R}_{il}$ and $\hat{C}_{il}$ represent the real and complex parts of the modal response predicted by the MTL-DNN, respectively; $x_{il,\tau}$ and $\hat{x}_{il}$ represent the input and reconstructed data, respectively. Note that the subscript τ is employed to indicate the corresponding terms are time-shifted to align them with the time sequence of the network's output. The last term in Eq. (15) represents a penalty condition for regularization, often referred to as a weight decay term [56]. This penalty involves applying the L2 norm to all the weights in the model with the purpose of avoiding gradient explosion and limiting over-fitting problems. The loss function L in Eq. (15) is minimized using the Adam algorithm [57], and adaptive gradient-descent backpropagation approach. On this basis, the updating of the weights of the network can be expressed as:

$$\begin{aligned} &m_q=\beta_1 m_{q-1}+\left(1-\beta_1\right)g_q,\quad \hat{m}_q=\frac{m_q}{1-\beta_1^q},\quad v_q=\beta_2 v_{q-1}+\left(1-\beta_2\right)g_p^2,\quad \hat{v}_q=\frac{v_q}{1-\beta_2^q},\\ &\theta_{q+1}=\theta_q-\frac{\alpha}{\sqrt{\hat{v}_q}+\epsilon}\hat{m}_q, \end{aligned} \tag{16}$$

where m_q and v_q represent the exponentially weighted moving averages of the gradients g_q and their squared values g_q^2 with respect to the parameters at iteration q, respectively. The terms $\hat{m}_q$ and $\hat{v}_q$ are the bias-corrected versions of m_q and v_q taking into account the initial biases and decay rates β_1 and β_2, respectively. The term θ_{q+1} stands for the updated weights at iteration $(q+1)$, which is calibrated considering a learning rate α. Finally, the term ϵ is a small constant added for numerical stability to avoid division by zero, typically set to 10^{-8}.

The hyper-parameters of the proposed MTL-DNN include the number of layers and neurons of the network, the decay rates β_1 and β_2, the learning rate α, and the weight decay parameter w_d. The number of layers (d,h) and neurons (f,g), as well as the learning rate and the dropout rates (percentage of eliminated neurons) of the regularization layers, are fine-tuned through manual trial and error depending of the specific case study. The decay rates β_1 and β_2 in the Adam algorithm are set to 0.9 and 0.9999, respectively, in accordance with common recommendations in the literature [58]. The activation functions used for all the hidden layers are set to hyperbolic tangent (tanh), except for the last two layers, which use linear activation. Finally, satisfactory generalization is achieved in all the considered case studies with a weight decay value w_d of 1E−4.

2.2.2. Modal parameter extraction

Once the MTL-DNN model is trained, the mode shapes are directly obtained as the weights between the penultimate and the last layers of the network (see Eq. (14)). It remains to determine the frequencies and damping ratios from the independent components $\mathbf{s}_i$, $1\le i\le n$. In this work, this is achieved by applying the SDOF Ibrahim Time-Domain (ITD) dynamic identification approach [59]. This approach starts by computing the free decay response for a particular component $\mathbf{s}_i$. Specifically, using the Natural Excitation Technique (NExT), the auto-correlation function $R_{s_i,s_i}(\tau)$ for a certain time-lag τ is obtained as:

$$R_{s_i,s_i}(\tau)=\mathbb{E}\left[s_i(t)s_i^{\mathrm{T}}(t+\tau)\right]=\mathscr{F}^{-1}\left[S_i(w)S_i(w)^*\right],\ \text{with}\ S_i(w)=\mathscr{F}\left[s_i(t)\right], \tag{17}$$

where the asterisk indicates the complex conjugate. On this basis, the time discrete free decay response obtained from Eq. (17) is organized into a Hankel matrix with four block rows and n_p columns as [60]:

$$\begin{bmatrix} R(1) & R(2) & \dots & R(n_p) \\ R(2) & R(3) & \dots & R(n_p+1) \\ \hdashline R(3) & R(4) & \dots & R(n_p+2) \\ R(4) & R(5) & \dots & R(n_p+3) \end{bmatrix}=\begin{bmatrix}\mathbf{R}_1\\ \hdashline \mathbf{R}_2\end{bmatrix}, \tag{18}$$

where the terms $R(k)$ correspond to the kth time samples of the auto-correlation function R_{s_i,s_i}, evaluated in a total of n_p samples. On this basis, it has been shown that the system matrix **T** can be obtained as [61]:

$$\mathbf{T}=(\mathbf{T}_1+\mathbf{T}_2)/2, \tag{19}$$

with matrices $\mathbf{T}_1$ and $\mathbf{T}_2$ determined as:

$$\mathbf{T}_1=\mathbf{R}_2\mathbf{R}_1^{\dagger}=\mathbf{R}_1^{\mathrm{T}}(\mathbf{R}_1\mathbf{R}_1^{\mathrm{T}})^{-1},\ \mathbf{T}_2=\mathbf{R}_1\mathbf{R}_2^{\dagger}=\mathbf{R}_1\mathbf{R}_2^{\mathrm{T}}(\mathbf{R}_2\mathbf{R}_2^{\mathrm{T}})^{-1}. \tag{20}$$

with † denoting the pseudo-inverse. On this basis, the discrete time poles of the independent component, μ_i and μ_i^*, can be extracted as the eigenvalues of the system matrix **T**. These discrete time poles are related to the continuous ones as:

$$\lambda_i = \frac{\ln(\mu_i)}{\Delta t}, \tag{21}$$

from which the natural frequency and damping ratio (omitting the complex conjugate pole) can be obtained as:

$$f_i = \frac{|\lambda_i|}{2\pi}, \quad \xi_i = -\frac{\mathrm{Re}(\lambda_i)}{2\pi f_n}. \tag{22}$$

2.2.3. Elimination of spurious modes

The number of independent components n in the broadband frequency of interest is generally unknown beforehand. As a first approximation, the inspection of the eigenvalues of the covariance matrix of the observations may provide insight into the number of influential components. Nonetheless, some of these may not truly represent physical model but rather spurious or mathematical modes stemming from noise and identification errors. Hence, in any OMA algorithm, it is essential to discriminate between physical and spurious/mathematical modes. In this study, an automatic procedure is adopted involving the following steps:

(A) *Hard criteria (HC)*: Spurious/mathematical modes are first identified as those violating certain physically meaningful ranges in terms of frequency $f_i \in [f_{min}, f_{max}]$, damping ratio $\xi_i \leq \xi_{max}$, and modal complexity. The latter, known thanks the developed multi-task architecture of the network, can be appraised in terms of their modal phase collinearity (MPC). The MPC metric quantifies the level of linearity of the modal displacements of a complex mode $\boldsymbol{\varphi}$ in the complexity plane [62]. Denoting the real and imaginary parts of $\boldsymbol{\varphi}$ as $\boldsymbol{\varphi}_R$ and $\boldsymbol{\varphi}_C$, respectively, their covariances can be cast into the covariance matrix **S** given by:

$$\mathbf{S} = \begin{bmatrix} \boldsymbol{\varphi}_R^{\mathrm{T}} \boldsymbol{\varphi}_R & \boldsymbol{\varphi}_R^{\mathrm{T}} \boldsymbol{\varphi}_C \\ \boldsymbol{\varphi}_C^{\mathrm{T}} \boldsymbol{\varphi}_R & \boldsymbol{\varphi}_C^{\mathrm{T}} \boldsymbol{\varphi}_C \end{bmatrix} \in \mathbb{R}^{2\times 2}, \tag{23}$$

whose eigenvalues, denoted as λ_1 and λ_2, provide insights into the complexity of the mode shapes. On this basis, the MPC metric is defined as:

$$\mathrm{MPC}(\boldsymbol{\varphi}) = \left(\frac{\lambda_1 - \lambda_2}{\lambda_1 + \lambda_2}\right)^2, \tag{24}$$

which ranges from 0 (not collinear at all) and 1 (perfect collinearity). In this way, since too complex modes are often due to identification errors, these modes can be eliminated as spurious/mathematical modes by imposing a certain threshold $\mathrm{MPC}(\boldsymbol{\varphi}) \geq \mathrm{MPC}_{min}$.

(B) *Elimination of low influential components*: It is reasonable to assume that physical independent components will contribute more intensively to the observed data. This can be interpreted in energetic terms by inspecting the spectral density functions of the identified independent components. From this consideration, a non-dimensional energy contribution metric E_c is defined as:

$$E_c = \frac{\int_0^{f_{ny}} S_c(\mathbf{s}_i)\, \mathrm{d}f}{f_s\, S_{c,max}}, \tag{25}$$

where $S_c(\mathbf{s}_i)$ is the spectral density function of a certain independent components $\mathbf{s}_i$ evaluated in the frequency broadband ranging from 0 to f_{ny}, with f_{ny} denoting de Nyquist frequency, i.e. $f_{ny} = f_s/2$. The normalization term $S_{c,max}$ corresponds to the spectral density value at resonant peak. The energy metric in Eq. (25) permits ranking the identified components in terms of their overall contributions to the observed data, so allowing the elimination of the least influential ones as spurious/mathematical modes.

3. Numerical results and discussion

The effectiveness of the proposed MTL-DNN is illustrated through three different case studies: a theoretical dynamic system, a laboratory structure, and a real full-scale bridge. The first case study is a 5-DOFs spring–mass damped model serving as a control case study to validate the neural network. In addition, various levels of noise are included in the validation data-set to assess the robustness in the predictions. The second case study is a 3D laboratory steel frame instrumented with low-cost sensors. This case study offers a realistic scenario suitable for testing the proposed algorithm for the elimination of spurious/mathematical modes. The third case study is a real-world reinforced concrete bridge, the Montecastelli Bridge in Italy. The neural networks were trained in a server computer Intel® Core™ i9-11900K (CPU@3.5 GHz), and evaluated in a personal computer Intel® Core™ i7-10750H (CPU@2.60 GHz). The neural networks were coded using the open-source Python library PyTorch.

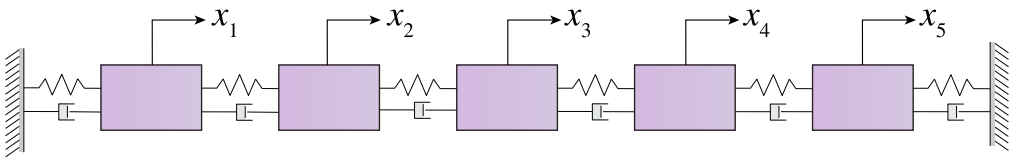

Fig. 3. Five DOFs linear spring–mass damped system.

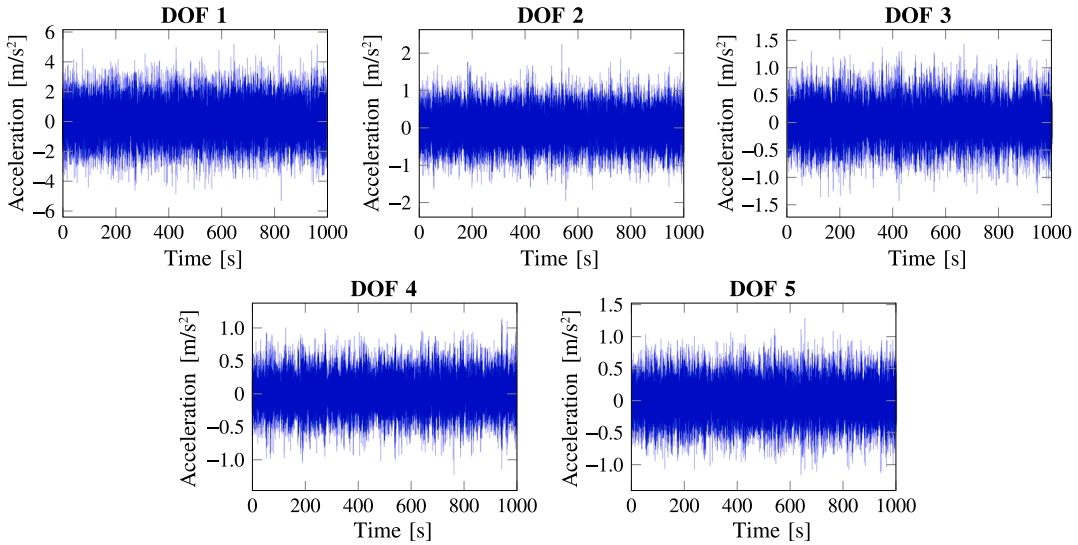

Fig. 4. Noise-free system response under stationary white Gaussian excitation for Case Study I: 5-DOFs system.

3.1. Case study I: Theoretical 5-DOFs system

The investigated 5-DOFs dynamic system shown in Fig. 3 is a benchmark case study used by several researchers in the literature (e.g. [41,42]). The structural matrices used in the model are:

$$\mathbf{M}=\begin{bmatrix}1&0&0&0&0\\0&2&0&0&0\\0&0&3&0&0\\0&0&0&4&0\\0&0&0&0&5\end{bmatrix},\ \mathbf{K}=100\times\begin{bmatrix}8&-8&0&0&0\\-8&24&-16&0&0\\0&-16&40&-24&0\\0&0&-24&56&-40\\0&0&0&-40&72\end{bmatrix},\ \mathbf{C}=\begin{bmatrix}3.5&-2.5&0&0&0\\-2.5&4.5&-2.0&0&0\\0&-2.0&3.2&-1.2&0\\0&0&-1.2&1.9&-0.7\\0&0&0&-0.7&2.7\end{bmatrix}, \tag{26}$$

where $\mathbf{M}\in\mathbb{R}^{5\times5}$ [kg] is the mass matrix, $\mathbf{K}\in\mathbb{R}^{5\times5}$ [N/m] is the stiffness matrix and $\mathbf{C}\in\mathbb{R}^{5\times5}$ [Ns/m] is defined as a non-proportional damping matrix. The system is excited at the 5-DOFs using stationary white Gaussian noises ($\sigma=1$ N). The system's responses are calculated using the Newmark-beta method with a time integration step of 1 ms (1000 Hz) and a time duration of 1000 s (1E+6 data-points), as shown Fig. 4. In this case study, the number of independent components is equal to the number of channels ($m=n=5$), thereby the algorithm for the elimination of spurious/mathematical modes is not applied herein.

3.1.1. Noise-free measurements

Fig. 5(a) furnishes the architecture of the MTL-DNN created for this case study. The learning rate, the batch size, and the dropout rate are set to 0.001, 200 and 30%, respectively. To generate the training data-set, the independent modal components are extracted from the raw acceleration time series by standard SOBI. The raw acceleration responses and the estimated independent components serve as inputs and outputs to build the data-set, considering an input/output time lag equal to 10 time samples ($\tau=10$ ms). All the weights of the network are randomly initialized, and the data-set is divided into training (80%), validation (10%), and test sub-sets (10%). The loss function in Eq. (15) is iteratively computed using forward propagation, followed by the updating of the weights using the Adam back-propagation algorithm. The training results are depicted in Fig. 5(b), where it is noted that the model convergence is optimally reached at epoch 100. In this case, the training of the DNN took 1 h and 25 min. It is important to remark that, while the initial SOBI takes 68 s, the source identification by MTL-DNN in the prediction step only takes 0.23 s. This represents a reduction of approximately 99.66%.

Recall that the outputs of the penultimate layer and the weights between the penultimate and the last layers directly provide the independent modal components $\mathbf{s}$ and the complex mode shapes $\boldsymbol{\Phi}$, respectively. Fig. 6 displays the five modal responses and their

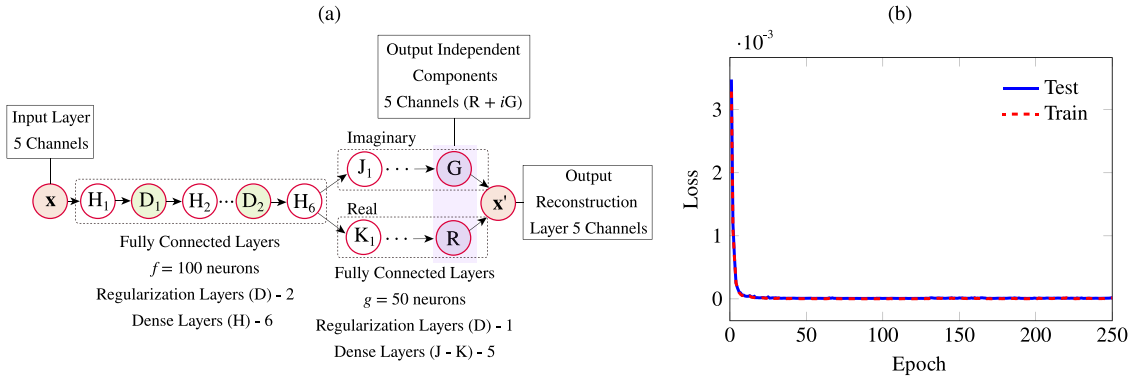

Fig. 5. MTL-DNN architecture (a) and convergence of the loss function (b) for Case Study I: 5-DOFs theoretical dynamic system.

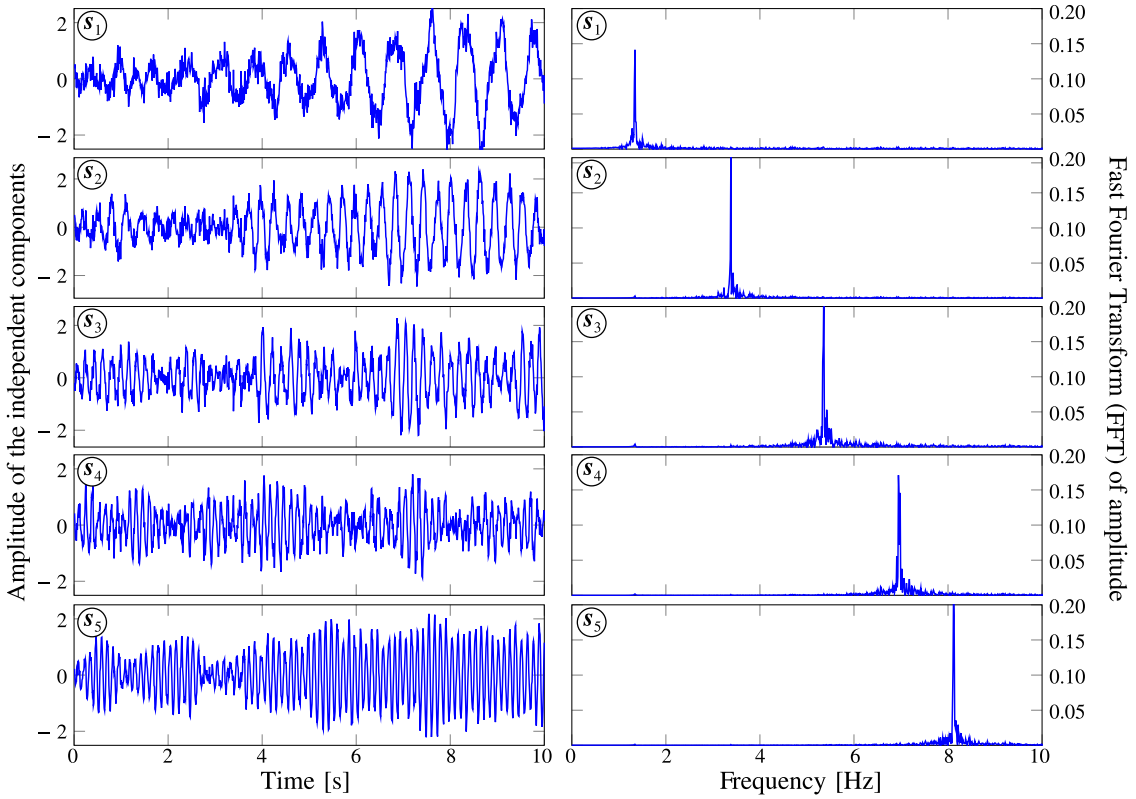

Fig. 6. Five independent components from s_1 to s_5 extracted using MTL-DNN without noise effects for Case Study I: 5-DOFs theoretical dynamic system.

Table 1
Comparison between the analytical and (noise-free) estimated modal parameters using MTL-DNN for Case Study I: 5-DOFs theoretical dynamic system.

Mode	Frequency [Hz]			Damping [%]		
	Analytical	MTL-DNN	Rel. Diff. [%]	Analytical	MTL-DNN	Rel. Diff. [%]
1	1.34	1.34	−0.04	1.34	1.30	−3.0
2	3.38	3.38	0.02	3.25	3.36	3.4
3	5.36	5.35	−0.01	3.50	3.44	−1.7
4	6.96	6.96	0.02	2.49	2.54	2.0
5	8.12	8.12	−0.01	1.22	1.27	4.1

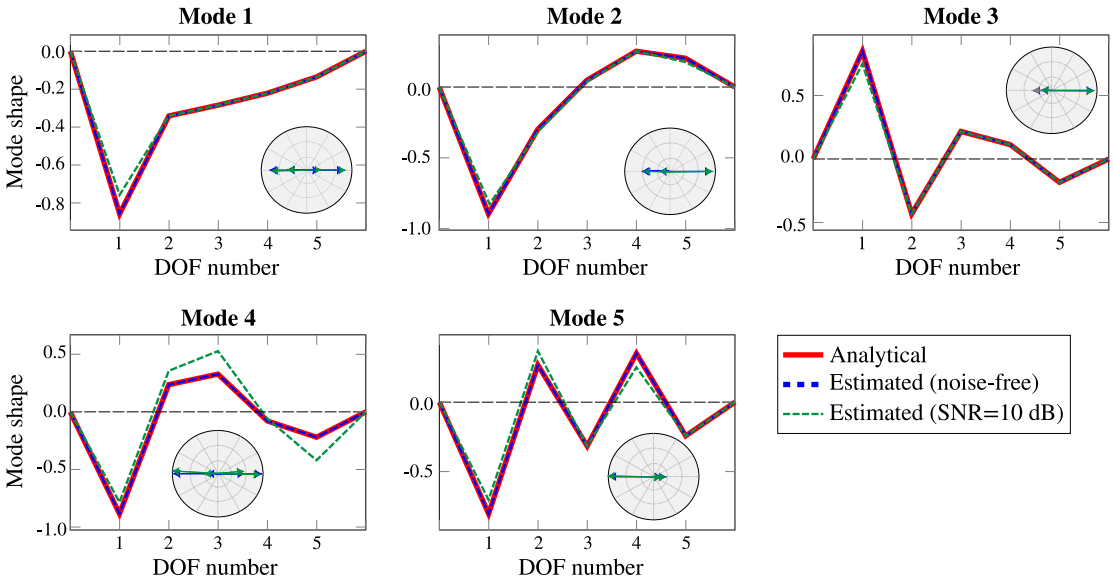

Fig. 7. Comparison between the analytical and the estimated mode shapes with (SNR = 10 dB) and without noise effects using the MTL-DNN for Case Study I: 5-DOFs theoretical dynamic system.

corresponding Fast Fourier Transforms (FFTs) estimated by the MTL-DNN. On this basis, the corresponding modal characteristics can be automatically extracted using the modal identification approach previously overviewed in Section 2.2.2. The resulting modal identification results and their comparison with the analytical results are reported in Table 1. These results reveal close agreements between the analytical results and the estimates by the MTL-DNN. Notably, the relative differences are exceptionally small in terms of frequencies, with a maximum value of 0.04%. However, when considering the damping ratios, it is important to acknowledge that a maximum error of 4.1% is found for Mode 5. Although this value may appear relatively high, it is essential to recognize the identification of damping ratios often involves considerable uncertainty in most OMA algorithms, as in this case when adopting the ITD method.

To gain a deeper understanding of the model's performance, Fig. 7 furnishes the mode shapes estimated as the weights between the last two layers of the MTL-DNN. The accuracy of these mode shapes is compared against the theoretical mode shapes using the Modal Assurance Criterion (MAC). Remarkably, the MAC values are all very close to 1.00, confirming an almost perfect correlation between the theoretical mode shapes and those estimated by the MTL-DNN. Note that the identified mode shapes are indeed complex-valued. This is particularly evident in the complexity plots of Modes 3, 4, and 5, for which MPC values of 97.8%, 95.8%, and 95.2% are obtained, respectively.

3.1.2. Robustness to measurement noise pollution

To demonstrate the robustness of the proposed MTL-DNN to measurement noise pollution, white noises of increasing magnitude are added to the input measurements. In Ref. [61], it is recommended that the minimum acceptable signal to noise-ratio (SNR) of acceleration acquisitions for OMA applications should be in higher than SNR = 40 dB. The SNR has the following definition:

$$\text{SNR (dB)} = 20\log_{10}\left(\frac{S_s}{S_n}\right), \tag{27}$$

where S_s and S_n are the amplitude of the signal $\mathbf{x}$ and the background noise, respectively. In this way, three noise levels are added to the observed measurements with values of SNR = [30, 20, 10] dB. For these analyses, the same architecture and hyper-parameters defined in the previous analysis are adopted herein.

Table 2 shows the modal characteristics obtained from the MTL-DNN predictions under the three considered noise levels. Notably, the relative differences in terms of frequencies and damping ratios do not exceed 2% and 5%, respectively. Furthermore, as the noise level increases, so do the errors with respect to the SOBI estimates. Specifically, for the highest noise level (SNR = 10 dB), maximum errors of 6.37% and 13.94% with respect to the SOBI estimates are obtained in terms of frequencies and damping ratios, respectively. Fig. 8 shows the analysis of the mode shapes, where similar conclusions are extracted. The mismatch between the SOBI estimates and the predictions by the MTL-DNN increases for increasing noise levels, with average traces of the MAC matrices in Fig. 8 of [1.00,0.99,0.96] for SNR= [30, 20, 10] dB respectively.

From the results of this first case study, it can be concluded that the proposed MTL-DNN model offers robust quasi-instantaneous modal identification capabilities. Importantly, unlike previous similar AI-BSS techniques reported in the literature, the proposed model allows estimating the complex-valued mode shapes, offering a comprehensive modal identification. It is important to emphasize that, once the hyper-parameters are set up, the whole process is automatic with no need for human intervention.

Table 2
Estimated modal parameters considering different noise levels with SNRs of [30, 20, 10] dB by means of SOBI and MTL-DNN for Case Study I: 5-DOFs theoretical dynamic system.

Frequency [Hz]										
Mode	Analytical	SNR = 30 dB			SNR = 20 dB			SNR = 10 dB		
		SOBI	MTL-DNN	Rel. Diff. [%]	SOBI	MTL-DNN	Rel. Diff. [%]	SOBI	MTL-DNN	Rel. Diff. [%]
1	1.34	1.35	1.36	0.93	1.35	1.33	−1.11	1.35	1.32	−1.78
2	3.38	3.42	3.44	0.64	3.42	3.40	−0.67	3.42	3.39	−1.00
3	5.35	5.40	5.37	−0.61	5.27	5.23	−0.75	5.55	5.50	−0.95
4	6.96	7.03	7.09	0.78	6.94	6.89	−0.73	6.82	6.77	−0.77
5	8.12	8.14	8.20	0.63	8.08	7.99	−1.20	8.13	7.98	−1.87
Damping ratios [%]										
1	1.26	1.26	1.27	0.79	1.27	1.29	1.57	1.27	1.31	3.15
2	3.45	3.45	3.46	0.29	3.45	3.42	−0.87	3.46	3.52	1.73
3	3.41	3.41	3.44	0.88	3.43	3.44	0.29	3.44	3.49	1.45
4	2.53	2.53	2.55	0.79	2.54	2.51	−1.18	2.53	2.41	−4.74
5	1.36	1.36	1.36	0.03	1.35	1.37	1.48	1.38	1.42	2.90

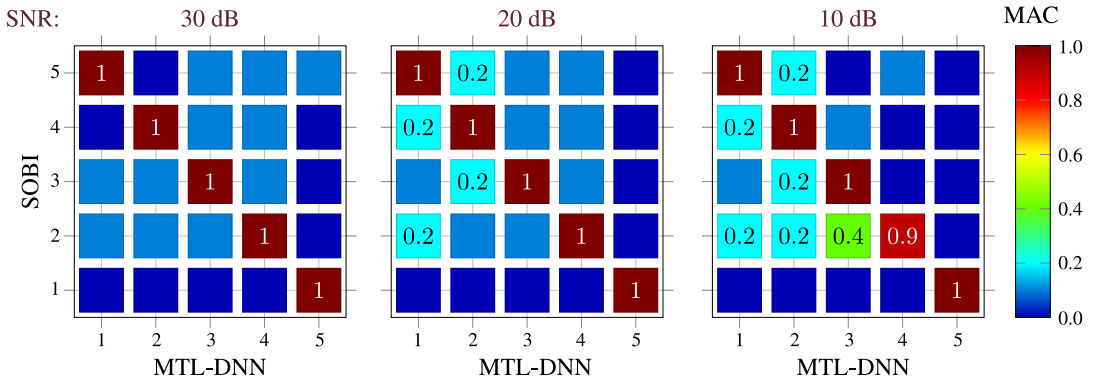

Fig. 8. Comparison in terms of MAC values between the theoretical and estimated modes shapes by MTL-DNN for Case Study I: 5-DOFs theoretical dynamic system, considering decreasing SNRs.

3.2. Case study II: Experimental three-dimensional steel frame

In this second case study, the proposed MTL-DNN is applied to a five-story laboratory steel frame with rigid joints and a total height of 1.4 m (each level - 0.28 m), located in the *Sustainable Structural Engineering laboratory* at the University of Granada (Fig. 9(a)). The monitoring system comprises 10 low-cost triaxial MEMS accelerometers model MPU-9250 (Resolution: 14 bit (0.6μT/LSB), Scale range: ±2 g/4 g/8 g/16 g, Noise Power Spectral Density: 300 $\mu g\sqrt{Hz}$) installed on the five floors of the frame as shown Fig. 9(c). At each level, accelerations are acquired by three channels: two in the x-direction and one in the y-direction. This amounts to a total of 15 channels labeled with C1 to C15. Such a configuration is aimed at characterizing the rigid diaphragm motions of the floors and the global torsional modes of the frame. Two multiplexers model PCA9548A are located on the third floor of the frame (see Fig. 9(e)), for the I2C data transmission of the 10 digital accelerometers (5 sensors per multiplexer). To generate a sufficient excitation level for successful modal identification, a 12 V DC motor with an eccentric mass of 82 grams (see Fig. 9(d)) is located on the upper floor of the structure. The motor is randomly activated and deactivated by an independent Arduino Nano micro-controller, and its speed is also randomly varied to simulate random excitations. The acceleration signals are recorded with sampling frequency of 100 Hz using a Raspberry Pi 3 Model B (see Fig. 9(b)) placed on the third level of the frame. Thirty minutes-long acceleration acquisitions are stored in an hourly basis in separate computer files, which are then sent automatically to a Google Drive repository. All the electronics are fixed to the frame through plastic 3D-printed supports. This case study offers a realistic framework to appraise the effectiveness of the algorithm for the elimination of spurious/ mathematical model previously introduced in Section 2.2.3.

In this case study, the number of independent components is set equal to the number of measurement channels (i.e. $n = m = 15$) with the purpose of appraising the effectiveness of the proposed spurious/mathematical modes elimination approach. The architecture of the MTL-DNN shown in Fig. 10(a) is quite similar to that of the previous case study. In this case, a total of 18 dense layers are defined (7 more compared to the network for Case Study I), including a larger number of neurons to accommodate the more complex dynamics of this case study. The accelerations file used for training the MTL-DNN corresponds to the first 30-min long acquisition (167,635 samples) recorded on April 27th, 2023 at 10:30 PM (CEST). Similarly to the previous case study, the raw acceleration data and the identified independent components by SOBI are used to form the data-set to train the network, which is

divided into training (80%), validation (10%), and test sub-sets (10%). All the weights of the network are initialized randomly, and the learning rate, the batch size and the dropout rate are set to 0.01, 250, and 35%, respectively. The size of the input/output time lag is set to 15 time samples ($\tau = 0.15$ s). The convergence of the training process is approximately achieved at epoch 100 as shown in Fig. 10(b). In this case, the training of the DNN took 1 h and 48 min. Notably, while SOBI takes 129 s, the prediction step of the modal separation by MTL-DNN only takes 0.56 s (reduction of ≈99.57%).

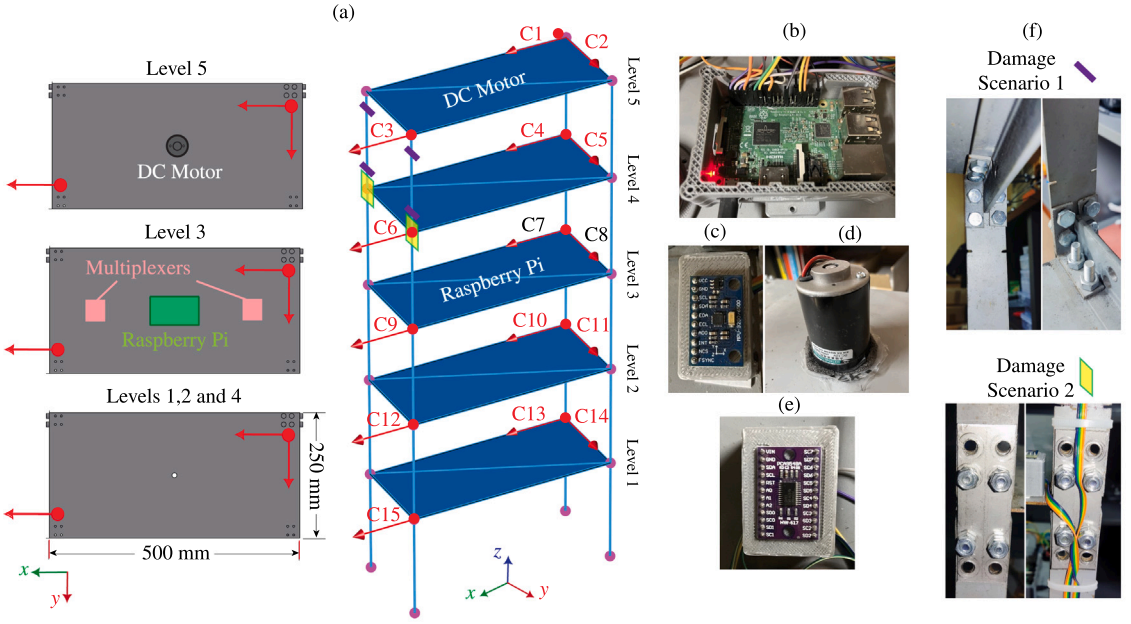

Fig. 9. Case Study II: Laboratory steel frame. Dimensions and sensors layout (a), Raspberry Pi 3 Model B (b), MEMS accelerometer MPU-9250 (c), DC motor (d) and multiplexer PCA9548A (e). (f) Damage Scenario 1 – June 5th: 23% reduction of the cross-sectional area of 2 columns between levels 4 and 5; Damage Scenario 2 – June 9th: Removal of outer bolts of two joints at level 4.

Once the 15 independent components are obtained after the MTL-DNN converges, it is necessary to determine those that truly represent physical modes of the frame. Table 3 reports the modal parameters identified after the ITD identification of the independent components (frequency and damping ratio), along with their corresponding MPC and energy contribution values. In this case study, the hard criteria included $f_{min} = 2$ Hz, $f_{max} = 25$ Hz, $\xi_{max} = 10\%$ and $\text{MPC}_{min} = 80\%$, resulting in a total of 8 components. Note that, in this case, these correspond to the 8 components with highest energy contribution factors S_c. The mode shapes for the selected 8 independent components are furnished in Fig. 11. It is apparent in this figure that the identified mode shapes correspond to global modes of vibration of the frame, including 7 lateral bending modes and one first-order torsional mode. The modes have been labeled with $i\text{F}d$, where i and d denote the order and the main direction (x, y, or z–torsion) of the motion, respectively. Additionally, the MAC values between the mode shapes identified by SOBI against those by MTL-DNN are also included in this figure. The diagonal of the MAC matrix shows values of 1, while the off-diagonal elements have values very close to zero. This indicates an almost perfect correlation between the mode shapes identified by SOBI and MTL-DNN. With regard to the MPC values in Table 3, note that modes

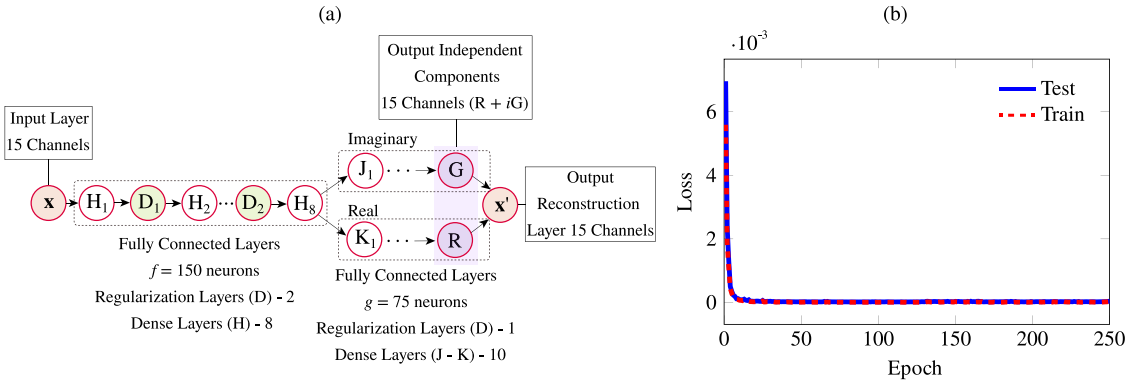

Fig. 10. MTL-DNN architecture (a) and convergence of the loss function (b) for Case Study II: Laboratory steel frame.

Table 3
Modal properties of the identified independent components (April 27th, 2023 10:30 PM (CEST)) by MTL-DNN for Case Study II: Laboratory steel frame.

Mode	Label	Frequency [Hz]	Damping ratio [%]	MPC [%]	E_c [–]
–	–	0.01	0.14	37.9	1.8
–	–	0.03	0.02	41.9	2.5
1	Fx	2.70	0.37	97.8	25.0
2	Fy	4.36	1.02	98.8	70.8
–	–	7.29	0.43	73.9	3.3
3	Fz	7.74	0.91	84.3	35.3
4	2Fx	8.18	0.58	97.6	41.1
5	3Fx	12.87	0.45	91.5	38.5
–	–	16.16	0.55	72.4	5.1
6	4Fx	16.58	0.43	84.5	27.2
7	5Fx	18.72	0.49	90.2	15.7
–	–	19.02	0.57	79.5	1.99
8	2Fy	20.72	0.57	82.3	21.1
–	–	23.15	0.47	65.4	1.6
–	–	26.81	0.63	58.0	7.2

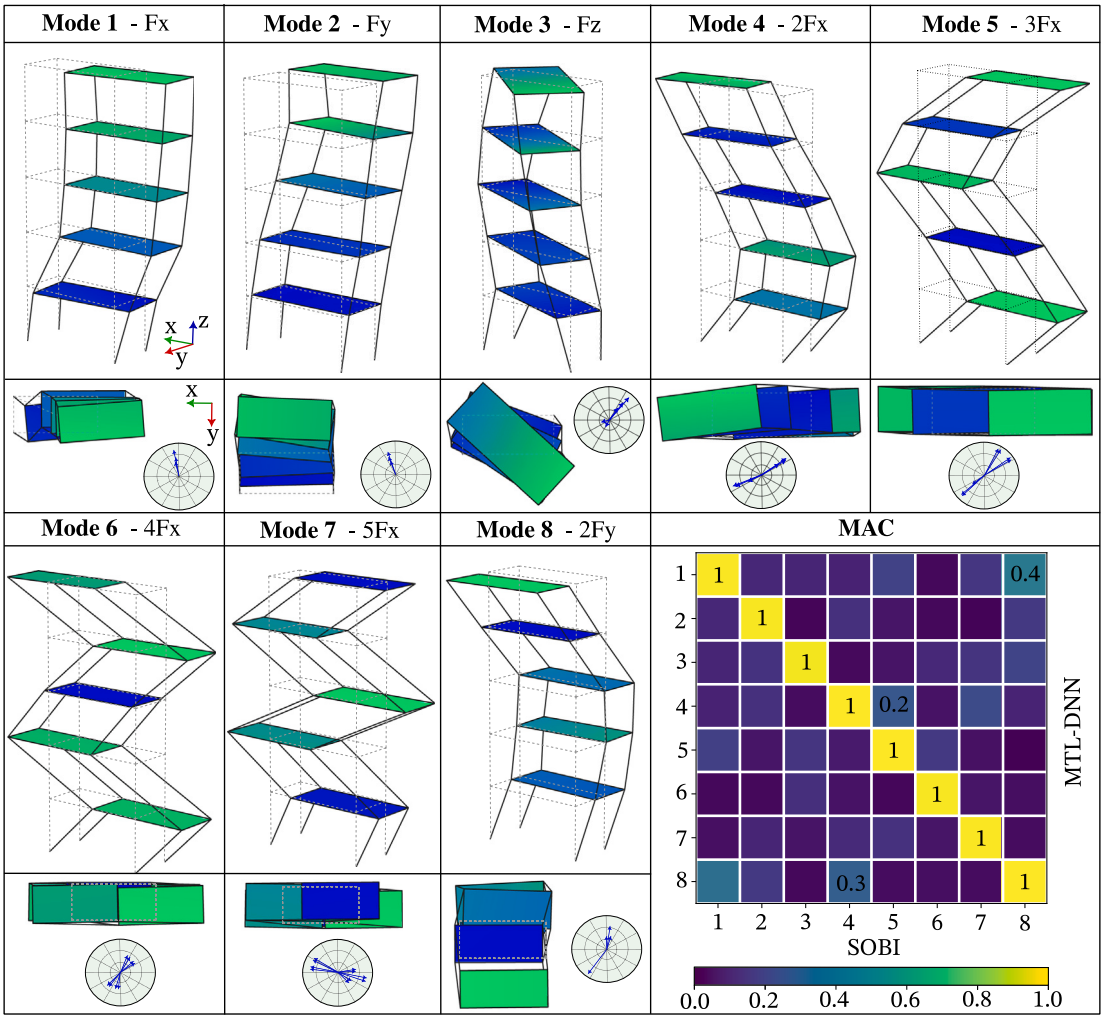

Fig. 11. Mode shapes of the laboratory steel frame estimated by MTL-DNN and MAC matrix with respect to the estimates by SOBI.

Fx, Fy, 2Fx, 3Fx and 5Fx, exhibit MPC values very close to 100%, with a minimum of 90.2%. This circumstance indicates that these modes are eminently real. Conversely, the remaining modes exhibit moderate complexity, with a minimum MPC value of 82.3%.

Table 4
Comparison of modal parameters (April 27th, 2023 10:30 PM (CEST)) estimated using SOBI and CoV-SSI versus the estimates by MTL-DNN for Case Study II: Laboratory steel frame.

Label	SOBI				CoV-SSI			
	Freq. [Hz]	Rel. Diff. [%]	Damp. [%]	Rel. Diff. [%]	Freq.[Hz]	Rel. Diff. [%]	Damp. [%]	Rel. Diff. [%]
Fx	2.70	−0.01	0.38	−2.63	2.70	0.01	0.38	−2.63
Fy	4.36	0.00	1.02	0.00	4.36	0.01	1.00	2.00
Fz	7.74	0.01	0.89	2.25	7.78	−0.49	0.87	4.60
2Fx	8.18	0.00	0.57	1.75	8.19	−0.01	0.56	3.57
3Fx	12.86	0.02	0.45	4.88	12.85	0.11	0.46	−2.17
4Fx	16.59	−0.04	0.41	−2.00	16.60	−0.08	0.42	2.38
5Fx	18.71	0.02	0.50	−1.72	18.86	−1.27	0.46	6.52
2Fy	20.71	0.03	0.56	0.22	20.68	0.20	0.52	9.62

These complexity levels may be attributed to non-linearities induced by conceivably semi-rigid joints of the frame. Additionally, the low sensitivity and SNR of the utilized low-cost MEMS sensors may also contribute.

The modes of vibration identified as physical are compared against the estimates by SOBI and CoV-SSI in Table 4. For the CoV-SSI, the automated algorithm implemented in the in-house software code P3P [63] has been employed. In this algorithm, the time lag used for the estimation of the Toeplitz matrix of the cross-correlations between the sensors has been set to 1 s, and the system matrices and the corresponding modal features have been estimated considering model orders varying from 40 to 60 with steps of 2. In this case, the identification of stable poles is conducted through a stabilization diagram. To this aim, the certainly spurious/mathematical poles are identified considering a set of hard criteria, including ζ_{max}, MPC_{min} and maximum Mode Phase Deviation (MPD_{max}) with values of 8%, 80%, and 60%, respectively. Subsequently, the possibly physical (stable) poles in the stabilization diagram are identified through a set of soft criteria, including tolerances in terms of resonant frequencies, damping ratios and MAC values of 0.05, 0.10 and 0.03, respectively. Finally, the physical poles of the system are identified through a hierarchical clustering algorithm following the automated procedure described in Ref. [63]. Note in Table 4 that, since the MTL-DNN model has been trained using SOBI, the error is smaller in this case. Specifically, maximum discrepancies of 0.02% and 0.49% are found between these two approaches in terms of frequencies and damping ratios, respectively. The discrepancies are larger when comparing with the estimates by CoV-SSI error, with maximum values of 0.05% and 0.73% in terms of resonant frequencies and damping ratios, respectively. Nonetheless, such discrepancies are far below the intrinsic uncertainties of most OMA techniques, thereby these results confirm the high accuracy of the proposed MTL-DNN. Furthermore, the low computational time required in the modal identification by MTL-DNN represents a key advantage. Specifically, the calculation time required by MTL-DNN to conduct the modal identification of the laboratory frame is only 0.66 s, which is almost negligible compared to the 129 s (reduction of ≈99.49%) and 87 s (reduction of ≈99.24%) required by SOBI and CoV-SSI, respectively.

3.2.1. Continuous modal parameter identification from MTL-DNN predictions

In this section, the acceleration data collected in the laboratory frame from April 26th until June 13th, 2023, are processed to assess the effectiveness of the proposed MTL-DNN approach for continuous modal identification. This data-set comprises a total of 710 acceleration records, each one with a duration and acquisition interval of 30 and 60 min, respectively. In this data-set, two different damage scenarios were performed on the frame on June 5th and 9th to test the potential of the proposed MTL-DNN approach for damage identification. The first damage scenario consists of a 23% reduction of the cross section at both endings of the columns between levels 4 and 5 using a cutting saw, while the second scenario consists of removing the outer bolts of two joints of level 4, as shown in Fig. 9(f).

To minimize the influence of frequencies outside the range of interest, a band-pass filter with cut-off frequencies 2 Hz and 21 Hz has been applied to the acceleration time series. A specialized network is considered in these analyses, focusing solely on the 8 independent components identified as physically meaningful in the prior study. The architecture of this network is defined with the same hyper-parameters and the same identical architecture, with the only difference that the input layer and the last two layers of the network have 8 neurons. In this case, the first three 30-min acquisitions (540,000 samples) were considered in the training data-set, resulting in a training time duration of 2 h and 33 min. This consideration proved crucial for achieving effective network generalization and predicting the variability in the modal properties of the frame driven by the environmental conditions (when used beyond the training phase), as reported below. The subsequent automated post-processing involves the extraction of the complex mode shapes and modal characteristics using the ITD approach, followed by the elimination of spurious/mathematical modes. Finally, to track the 8 physical modes throughout the whole monitoring period, a simple modal tracking algorithm was adopted. The main purpose of the modal tracking algorithm is to match the identified poles with the modal reference baseline previously reported in Table 3. Additionally, it aims to eliminate potential residual spurious/mathematical modes that may arise due to identification errors. To achieve this, the poles extracted after each identification are compared to the reference baseline, retaining those that meet a set of threshold criteria, including relative differences in terms of frequency of 0.10 and MAC values of 0.70.

The identified time series of resonant frequencies are depicted in Fig. 12. The aforementioned modal tracking approach eliminated only a limited number of residual spurious/mathematical poles, with the majority of the identified modes meeting the tracking thresholds. This resulted in identification success ratios exceeding 90% across all the modes. For comparison purposes,

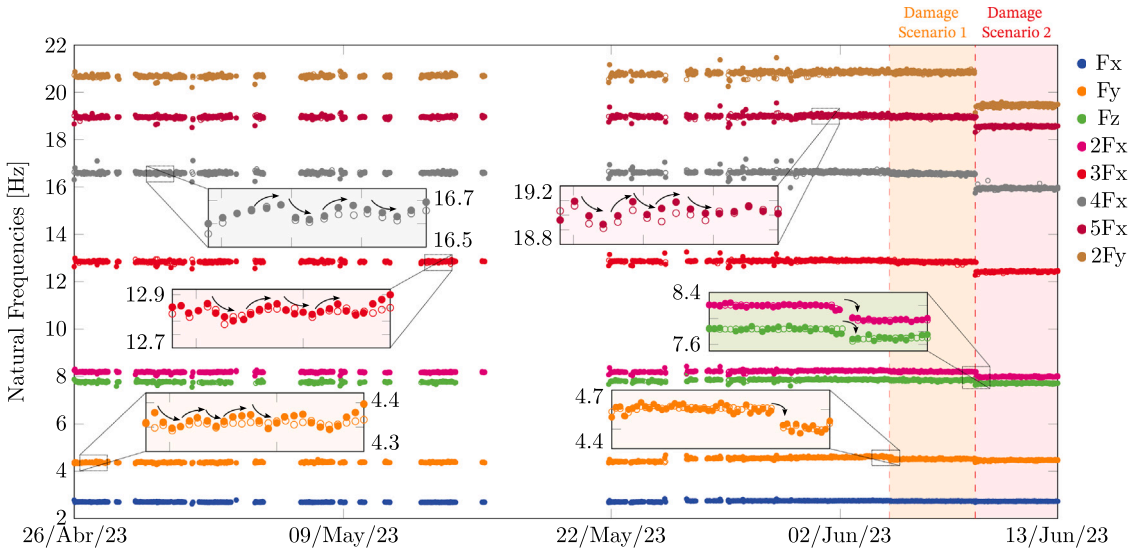

Fig. 12. Tracking of the resonant frequencies of the laboratory steel frame from April 26th until June 13th 2023. Filled and open dots represent the estimates by MTL-DNN and CoV-SSI, respectively.

the identification results extracted by automated CoV-SSI are also included, employing the same identification parameters as in the previous section. In this case, due to the considerable shifts in the time series induced by the considered damage scenarios, a multi-stage modal tracking and tight tolerance criteria of 0.05 and 0.85 in terms of frequency and MAC values were deemed critical to obtain the results in Fig. 12. This approach involves considering different modal baselines for the healthy period, and the two damage scenarios. This necessity is justified by the fact that the CoV-SSI identifies a higher number of poles after the automated interpretation of the stabilization diagrams following every acquisition. This results in a considerable number of spurious poles that need to be filtered out by the modal tracking algorithm. In contrast, the developed neural network provides only 8 poles per acquisition, allowing for the relaxation of the tracking tolerances. It is important to mention that the time gaps visible in the figure are not the result of errors in the identification, but rather to interruptions in the power supply of the monitoring system. Overall, the close agreement between the two approaches demonstrates the accuracy of the proposed approach. In both cases, the presence of certain oscillations induced by variations in environmental temperature/humidity conditions is noticeable, as depicted in the zoom views in Fig. 12. More interestingly, it is evident in Fig. 12 that the proposed MTL-DNN is capable of tracking the damage-induced variations with high accuracy, despite being trained exclusively on data from the healthy condition of the frame. Indeed, these damage scenarios can be considered moderate to severe, with mean frequency decays of −0.42% and −2.17%, and MAC values of 0.94 and 0.92 for Scenarios 1 and 2, respectively, with respect to the healthy baseline of the frame. Indeed, given the considerable shifts in the modal properties induced by damage, a multi-stage modal tracking approach considering different modal baselines for the healthy condition and the two damage scenarios was required to accurately track the modes of the frame using CoV-SSI. Instead, the proposed MTL-DNN model provided direct tracking of the modes with one single reference baseline. This aspect represents another key advantage of the proposed model, requiring no expert intervention once the network is trained. Finally, these analyses underscore that the actual computational advantage of the proposed MTL-DNN arises when adopted for periodic dynamic identification in continuous SHM schemes. This advantage becomes apparent after the DNN is trained, as its evaluation time is markedly lower than that of standard OMA techniques. In particular, while the CoV-SSI required 1 h and 35 min to process the entire data-set, the MTL-DNN model completed the analysis in just 29 min, representing a time reduction of 69.47%.

3.3. Case study III: Montecastelli bridge

This third case study investigates the effectiveness of the proposed MTL-DNN for modal identification applied to a real-world in-operation structure–the Montecastelli Bridge. Situated between the municipalities of Città di Castello and Umbertide in the Umbria region of central Italy, the Montecastelli Bridge is a 68.8-m-long concrete bridge that spans the Tiber River. The bridge was constructed to replace a multi-span stone arch bridge that suffer significant damage during World War II. The original bridge consisted of three consecutive arches, with one pylon submerged in the river and the other in the floodplain. After the war, the two spans over the river were replaced by a single reinforced concrete arch span, resulting in the current configuration with no pylons in the river. The two twin arches, each spanning 68.7 m with a rise of approximately 13 m, are composed of two elements with variable cross-section connected by transverse girders. They support the concrete deck through vertical struts. The width of the masonry arch on the north side aligns with the planar distance between the twin arches. Consequently, the longitudinal girders of the deck extend approximately 1 m beyond the vertical struts and rest on the cantilever ends of the transverse girders. For visual reference, Fig. 13(a) shows two photographs of the bridge taken in 1955 and 2012.

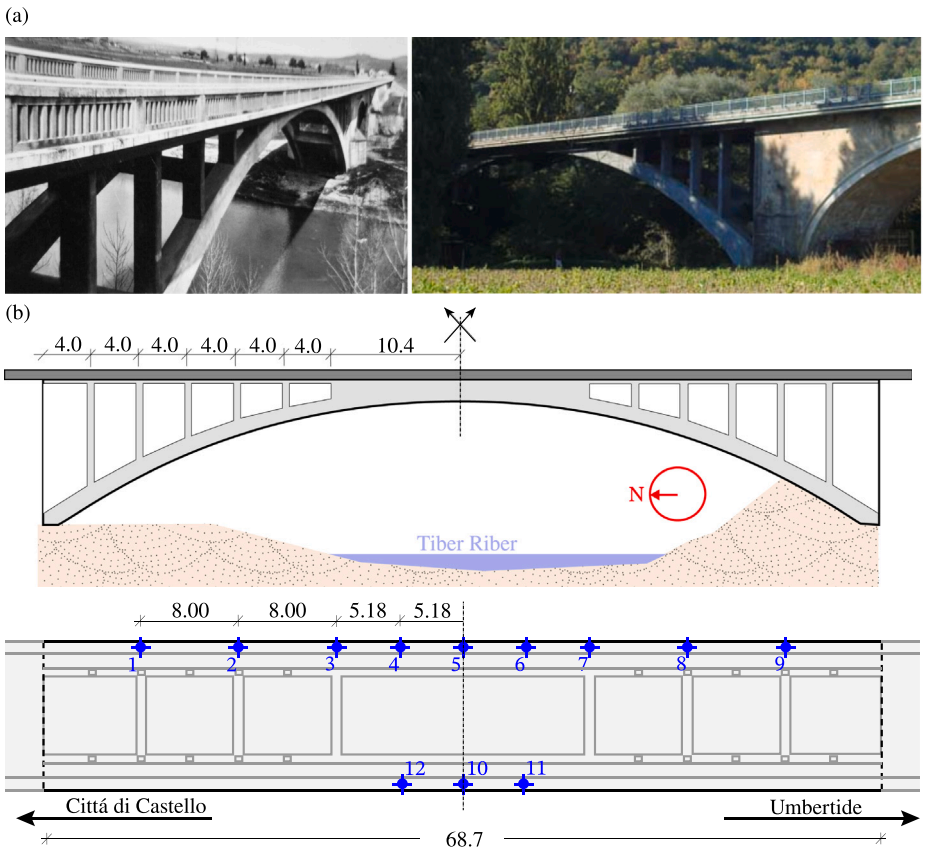

Fig. 13. (a) Views of the Montecastelli Bridge (left: photography from 1955, Source: paesi.altervista.org; right: photography from 2012, Source: [64]). (b) Plan and elevation views of the Montecastelli Bridge with the sensors layout (dimensions in m).

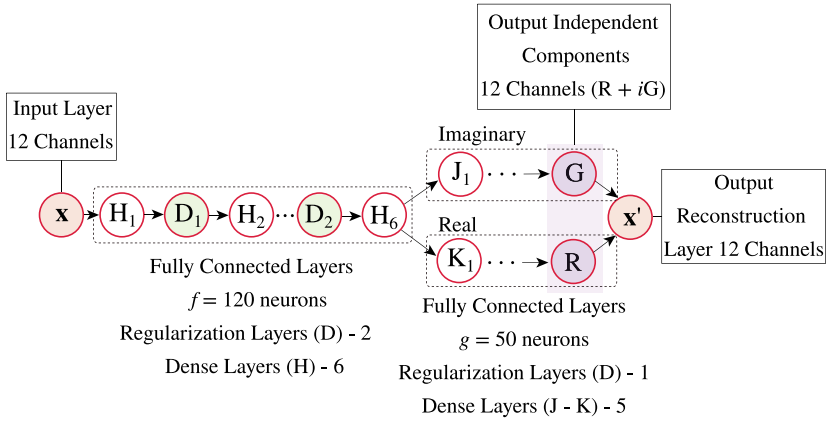

Fig. 14. MTL-DNN architecture for Case Study III: Montecastelli Bridge.

With the objective of identifying the dynamic characteristics of the bridge, an ambient vibration test (AVT) was carried out on February 22nd, 2012, as documented in Ref. [64]. The monitoring system comprised 12 uni-axial piezoelectric accelerometers (model WR 731A, 10 V/g) monitoring the vertical accelerations at 9 cross-sections of the bridge, as depicted in Fig. 13(b). In the three cross-sections located at mid-span of the bridge, the sensors were placed on both sides of the deck, while in the remaining six sections, the sensors were placed only on the east side of the deck. Each sensor was linked by a short cable (1 m) to a WR P31 power unit/amplifier, which supplied the continuous current required to run the accelerometer's internal amplifier. A 24-channel

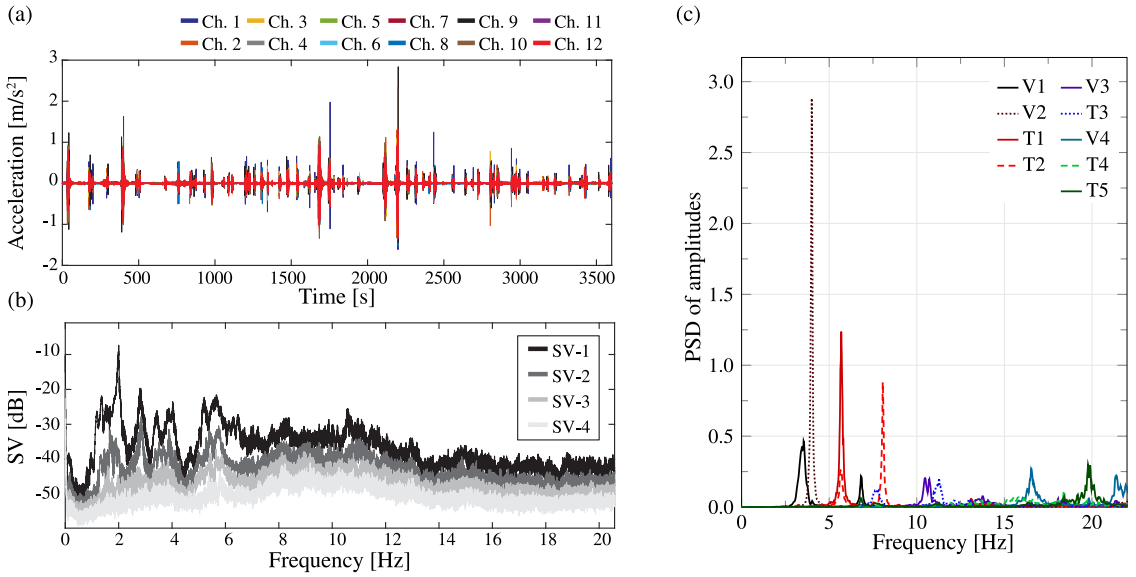

Fig. 15. Ambient acceleration records (a), first four singular values (SVs) of the spectral density matrix of accelerations (b), and independent components extracted using MTL-DNN (c) for Case Study III: Montecastelli Bridge (acquisitions carried out on February 22nd, 2012, 11.00 AM (CEST).

Table 5
Comparison between the modal parameters estimated using MTL-DNN against the estimated by CoV-SSI and Data-SSI [64] for Case Study III: Montecastelli Bridge (acquisitions carried out on February 22nd, 2012, 11.00 AM (CEST).

Label	MTL-DNN			CoV-SSI				Data-SSI [64]			
	f_i [Hz]	ξ_i [%]	E_c [–]	f_i [Hz]	Rel. Diff. [%]	ξ_i [%]	Rel. Diff. [%]	f_i [Hz]	Rel. Diff. [%]	ξ_i [%]	Rel. Diff. [%]
V1	3.41	1.92	13.6	3.41	0.02	1.85	3.78	3.41	0.08	1.79	7.26
V2	4.00	0.81	35.6	4.00	0.02	0.79	2.53	4.00	−0.04	0.75	8.00
T1	5.69	1.20	26.1	5.69	−0.01	1.19	0.84	5.71	−0.31	1.16	3.45
T2	6.84	1.15	22.5	6.84	−0.01	1.18	−2.54	6.83	0.02	1.24	−7.26
V3	7.76	1.41	53.9	7.76	−0.01	1.41	0.00	7.76	−0.02	1.32	6.82
T3	8.03	0.81	34.7	8.03	−0.02	0.80	1.25	8.03	0.02	0.87	−6.90
V4	10.42	1.05	14.3	10.41	0.02	1.04	0.96	10.41	0.03	0.98	7.14
T4	11.15	1.83	16.2	11.15	0.00	0.81	2.47	11.15	0.01	0.77	7.79
T5	13.84	1.12	7.0	13.84	−0.01	1.11	0.90	13.84	0.01	–	–

data acquisition system (24 bit resolution, 102 dB dynamic range, and anti-aliasing filters) was used to record 30 min ambient accelerations at a sampling frequency of 100 Hz. That acquisition data (shown below in Fig. 15(a)) are retrieved in this work to appraise the accuracy of the developed MTL-DNN approach and benchmark it against other state-of-the-art OMA techniques.

In the design of the network for this case study, the number of independent components to be determined is set equal to the number of sensors ($n = m = 12$). The architecture of the MTL-DNN, as shown in Fig. 14, is quite similar to the ones presented in the previous case studies. A total of 20 min of ambient accelerations (120,000 samples) are used as the training data-set, divided into training (80%), validation (10%), and test sub-sets (10%). The learning rate, the batch size and the dropout rate are set to 0.01, 250, and 35%, respectively. The size of the input/output time lag is set to 22 time samples ($\tau = 0.22$ s). The model convergences at epoch 100 (1 h and 53 min of training time), for which the modal separation in the prediction step takes 0.45 s.

Table 5 presents the modal parameters identified from the MTL-DNN predictions. A total of 9 components are obtained after applying the HC, including $f_{min} = 3$ Hz, $f_{max} = 14$ Hz, and $\text{MPC}_{\text{min}} = 85\%$. Notably, these modes also correspond to those with highest energy contribution factors S_c (the three components identified as spurious/mathematicals have S_c factors between 1.5 and 4.6). Fig. 15(b) and (c) show the singular values (SVs) of the spectral density matrix of accelerations and the PSD of the independent components identified as physical modes, respectively. After inspecting the modal displacements shown in Fig. 16, the components of interest in Table 5 have been labeled using “V” and “T” to denote the vertical bending and torsional modes, respectively. Specifically, four flexural modes (V1 to V4) and five torsional modes (T1 to T5) are identified. To assess the quality of the modal identification results by MTL-DNN, Table 5 reports its predictions with those obtained by CoV-SSI and Data-SSI (from Ref. [64]). It is noted that the predictions by MTL-DNN are considerably close to those by CoV-SSI, achieving maximum relative differences of 0.02% and 3.78% in terms of resonant frequencies and damping ratios, respectively. On the other hand, when comparing the estimates by MTL-DNN with those by Data-SSI, the relative differences in terms of resonant frequencies are considerably low, with a maximum value of 0.08%. However, discrepancies in terms of damping ratios are notably higher, with a maximum relative difference of 8.00%. Nonetheless, considering the frequent high uncertainty in estimating the damping ratios of

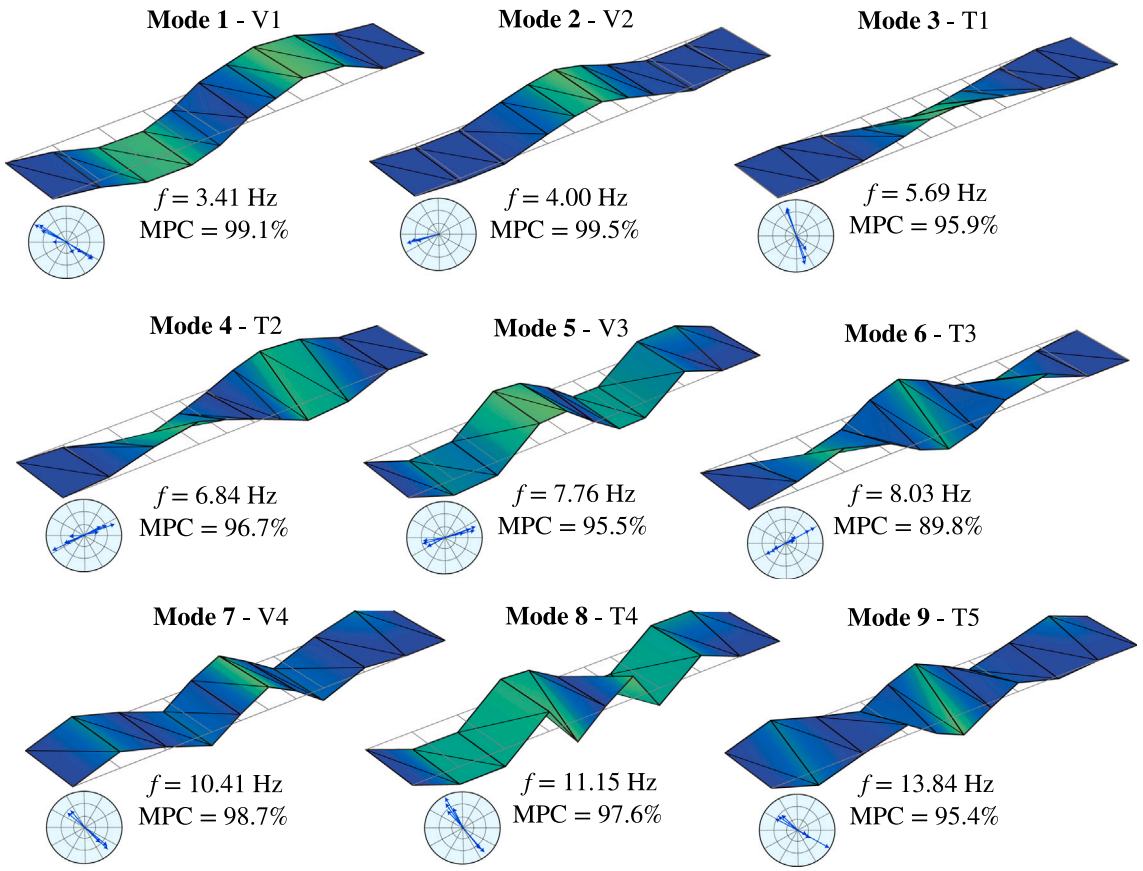

Fig. 16. Mode shapes estimated by the MTL-DNN model for Case Study III: Montecastelli Bridge.

low-excited structures, as is the case in this study, these results are considered satisfactory. These differences may arise as a result of certain limitations in the underlying SOBI technique. Specifically, note in Fig. 15(c) that some independent components are not purely harmonic, evidencing some deficiencies in the source separation. This is conceivably explained by the appearance of time-correlations between the modal displacements, possibly induced by the non-Gaussian traffic excitation. Despite these limitations, in all cases, the MAC values between the modes estimated by MTL-DNN and Cov-SSI/Data-SSI are very close to 1, demonstrating the high accuracy of the modal identification by MTL-DNN predictions. Finally, the results in Fig. 16 showcase the ability of the proposed MTL-DNN to identify complex mode shapes. In particular, mode T3 exhibits a considerably complex nature, with a MPC value of 89.8%. In summary, the study reveals consistent agreement between the modal signatures estimated by the proposed MTL-DNN and state-of-the-art OMA techniques, with the fundamental advantage of substantially lower computational demands.

4. Concluding remarks

This work has presented the development of a Multitask Deep Learning algorithm (MTL-DNN) for BSS quasi real-time modal identification structures. The architecture of the developed AI-BSS model is designed to extract both the real and complex parts of the modal displacements from raw ambient acceleration data as input, so allowing estimating complex-valued mode shapes and offering a comprehensive system identification. In the proposed approach, the complex mode shapes are extracted from the weights between the last layers of the network, while the resonant frequencies and damping ratios are extracted from the (complex) independent components using the SDOF Ibrahim time-domain identification method. Furthermore, an automated spurious/mathematical mode elimination algorithm based on several hard criteria have been introduced. The effectiveness of the developed approach has been evaluated through three case studies: (i) a theoretical 5-DOFs dynamic system, (ii) a laboratory steel frame, and (iii) a real-world in-operation bridge, the Montecastelli Bridge. The theoretical case study has served as a control study to validate effectiveness of the proposed approach and test its robustness to measurement noise. The laboratory frame has been investigated as a realistic scenario to test assess the developed spurious/mathematical mode elimination approach. Furthermore, continuous acceleration acquisitions in the frame from April 26th until June 13th, 2023, have been used to assess the capability of the proposed approach for conducting long-term OMA and damage identification. Interestingly, even though trained exclusively on data from the healthy condition of the frame, the proposed AI-BSS model accurately tracked the damage-induced variations in the modal properties of the frame. These

results demonstrate the generalization potential of the proposed approach, making it useful not only for novelty detection but also for damage identification. Finally, the Montecastelli Bridge has been studied as an instance of a real-world in-operation structure. In this case study, thorough comparison analyses with state-of-the-art OMA techniques have been reported to demonstrate high accuracy in the modal estimates by the proposed approach, with the fundamental advantage of minimal computational time demands. Overall, the presented results and discussion have demonstrated the potential of the proposed approach for performing rapid and automated modal identification of structures with minimal expert intervention.

Overall, the proposed AI-driven BSS model demonstrates high versatility and applicability to various structural systems, excelling in conducting fast and automated modal identification with minimal computational demands and human intervention. With further development and implementation, this innovative approach holds great potential for scalability within infrastructural networks, offering an efficient technique for condition-based maintenance and damage identification. Future developments include the application of the proposed architecture to more advanced BSS techniques capable of solving the under-determined mixing problem. Additionally, to address some of the identified deficiencies in the source separation for of non lightly-damped systems and non-perfectly Gaussian excitations, more sophisticated (non-Hermitian) diagonalization approaches will be explored. Finally, owing to its low computational demands, their implementation into miniaturized micro-controllers may hold great potential for quasi real-time online modal identification.

CRediT authorship contribution statement

Israel Alejandro Hernández-González: Investigation, Formal analysis, Resources, Software, Validation, Writing – original draft, Writing – review & editing. **Enrique García-Macías:** Investigation, Supervision, Writing – review & editing, Methodology, Writing – original draft. **Gabriele Costante:** Conceptualization, Investigation. **Filippo Ubertini:** Investigation, Supervision.

Declaration of competing interest

The authors declare that they have no known competing financial interests or personal relationships that could have appeared to influence the work reported in this paper.

Data availability

Data will be made available on request.

Acknowledgments

This work has been supported by the Spanish Ministry of Science and Innovation through the research project “BRIDGEXT - Life-extension of ageing bridges: Towards a long-term sustainable Structural Health Monitoring” (Ref. PID2020-116644RB-I00). F. Ubertini also acknowledges the support of the Italian Ministry of University and Research (MUR) through the funded project “TIMING - Tine evolution laws for improving the structural reliability evaluation of existing post-tensioned concrete deck Bridges” within the PNRR PRIN2022 Call (Proj. P2022 3Y947). Funding for open access charge: Universidad de Granada / CBUA.

References

[1] S. Hao, I-35W bridge collapse, J. Bridge Eng. 15 (5) (2010) 608–614.
[2] Gian Michele Calvi, Matteo Moratti, Gerard J O'Reilly, Nicola Scattarreggia, Ricardo Monteiro, Daniele Malomo, Paolo Martino Calvi, Rui Pinho, Once upon a time in Italy: The tale of the Morandi Bridge, Struct. Eng. Int. 29 (2) (2019) 198–217.
[3] Bundesanstalt für Straßenwesen, Zustandsnoten der Brücken, 2019.
[4] American Road and Transportation Builders Association (ARTBA), Annual bridge report, 2023.
[5] Claus Peter Fritzen, Vibration–based structural health monitoring–concepts and applications, in: Key Engineering Materials, Vol. 293, Trans Tech Publ, 2005, pp. 3–20.
[6] Filipe Magalhães, Álvaro Cunha, Explaining operational modal analysis with data from an arch bridge, Mech. Syst. Signal Process. 25 (5) (2011) 1431–1450.
[7] Edwin Reynders, Jeroen Houbrechts, Guido De Roeck, Fully automated (operational) modal analysis, Mech. Syst. Signal Process. 29 (2012) 228–250.
[8] William Soo Lon Wah, Y.T. Chen, Gethin Wyn Roberts, Ahmed Elamin, Separating damage from environmental effects affecting civil structures for near real-time damage detection, Struct. Health Monit. 17 (4) (2018) 850–868.
[9] Filippo Ubertini, Nicola Cavalagli, Alban Kita, Gabriele Comanducci, Assessment of a monumental masonry bell-tower after 2016 Central Italy seismic sequence by long-term SHM, Bull. Earthq. Eng. 16 (2) (2018) 775–801.
[10] S.K. Au, F.L. Zhang, Y.C. Ni, Bayesian operational modal analysis: theory, computation, practice, Comput. Struct. 126 (2013) 3–14.
[11] Wei Guan, L.L. Dong, J.M. Zhou, Yi Han, J. Zhou, Data-driven methods for operational modal parameters identification: A comparison and application, Measurement 132 (2019) 238–251.
[12] Fahad Bin Zahid, Zhi Chao Ong, Shin Yee Khoo, A review of operational modal analysis techniques for in-service modal identification, J. Braz. Soc. Mech. Sci. Eng. 42 (2020) 1–18.
[13] Carlo Rainieri, Giovanni Fabbrocino, Automated output-only dynamic identification of civil engineering structures, Mech. Syst. Signal Process. 24 (3) (2010) 678–695.
[14] Enrique García-Macías, Filippo Ubertini, MOVA/MOSS: Two integrated software solutions for comprehensive Structural Health Monitoring of structures, Mech. Syst. Signal Process. 143 (2020) 106830.
[15] Giacomo Zini, Michele Betti, Gianni Bartoli, A quality-based automated procedure for operational modal analysis, Mech. Syst. Signal Process. 164 (2022) 108173.

[16] Elisa Tomassini, Enrique García-Macías, Edwin Reynders, Filippo Ubertini, Model-assisted clustering for automated operational modal analysis of partially continuous multi-span bridges, Mech. Syst. Signal Process. 200 (2023) 110587.
[17] P.É. Charbonnel, Fuzzy-driven strategy for fully automated modal analysis: Application to the SMART2013 shaking-table test campaign, Mech. Syst. Signal Process. 152 (2021) 107388.
[18] P. Cheema, M. Makki Alamdari, G.A. Vio, F.L. Zhang, C.W. Kim, Infinite mixture models for operational modal analysis: An automated and principled approach, J. Sound Vib. 491 (2021) 115757.
[19] Marco Civera, Luigi Sibille, Luca Zanotti Fragonara, Rosario Ceravolo, A DBSCAN-based automated operational modal analysis algorithm for bridge monitoring, Measurement 208 (2023) 112451.
[20] E.M. Tronci, M. De Angelis, R. Betti, V. Altomare, Multi-stage semi-automated methodology for modal parameters estimation adopting parametric system identification algorithms, Mech. Syst. Signal Process. 165 (2022) 108317.
[21] Jérôme Antoni, Blind separation of vibration components: Principles and demonstrations, Mech. Syst. Signal Process. 19 (6) (2005) 1166–1180.
[22] Gaëtan Kerschen, Fabien Poncelet, J.-C. Golinval, Physical interpretation of independent component analysis in structural dynamics, Mech. Syst. Signal Process. 21 (4) (2007) 1561–1575.
[23] A. Sadhu, S. Narasimhan, J. Antoni, A review of output-only structural mode identification literature employing blind source separation methods, Mech. Syst. Signal Process. 94 (2017) 415–431.
[24] Aapo Hyvärinen, Erkki Oja, Independent component analysis: algorithms and applications, Neural Netw. 13 (4–5) (2000) 411–430.
[25] S.I. McNeill, D.C. Zimmerman, A framework for blind modal identification using joint approximate diagonalization, Mech. Syst. Signal Process. 22 (7) (2008) 1526–1548.
[26] Xiao-Jun Yao, Ting-Hua Yi, Shao-Wei Zhao, Blind modal identification for decentralized sensor network by modified sparse component analysis in frequency-domain subspace, Eng. Struct. 269 (2022) 114794.
[27] Yan Xu, James M.W. Brownjohn, David Hester, Enhanced sparse component analysis for operational modal identification of real-life bridge structures, Mech. Syst. Signal Process. 116 (2019) 585–605.
[28] Yongchao Yang, Satish Nagarajaiah, Time-frequency blind source separation using independent component analysis for output-only modal identification of highly damped structures, J. Struct. Eng. 139 (10) (2013) 1780–1793.
[29] Jianming Li, Tengfei Bao, Carlos E. Ventura, An automated operational modal analysis algorithm and its application to concrete dams, Mech. Syst. Signal Process. 168 (2022) 108707.
[30] Mohammad AlHamaydeh, Nour Ghazal Aswad, Structural health monitoring techniques and technologies for large-scale structures: Challenges, limitations, and recommendations, Pract. Period. Struct. Des. Constr. 27 (3) (2022) 03122004.
[31] Shiyin Wei, Xiaowei Jin, Hui Li, General solutions for nonlinear differential equations: a rule-based self-learning approach using deep reinforcement learning, Comput. Mech. 64 (2019) 1361–1374.
[32] Yuequan Bao, Zhiyi Tang, Hui Li, Compressive-sensing data reconstruction for structural health monitoring: a machine-learning approach, Struct. Health Monit. 19 (1) (2020) 293–304.
[33] Ying Lei, Yixiao Zhang, Jianan Mi, Weifeng Liu, Lijun Liu, Detecting structural damage under unknown seismic excitation by deep convolutional neural network with wavelet-based transmissibility data, Struct. Health Monit. 20 (4) (2021) 1583–1596.
[34] Zhiyi Tang, Zhicheng Chen, Yuequan Bao, Hui Li, Convolutional neural network-based data anomaly detection method using multiple information for structural health monitoring, Struct. Control Health Monit. 26 (1) (2019) e2296.
[35] Onur Avci, Osama Abdeljaber, Serkan Kiranyaz, Mohammed Hussein, Moncef Gabbouj, Daniel J Inman, A review of vibration-based damage detection in civil structures: From traditional methods to Machine Learning and Deep Learning applications, Mech. Syst. Signal Process. 147 (2021) 107077.
[36] Rosette Niyirora, Ji Wei, Elyse Masengesho, Jean Munyaneza, Ferdinand Niyonyungu, Ritha Nyirandayisabye, Intelligent damage diagnosis in bridges using vibration-based monitoring approaches and machine learning: A systematic review, Results Eng. (2022) 100761.
[37] Valentina Giglioni, Ilaria Venanzi, Valentina Poggioni, Alfredo Milani, Filippo Ubertini, Autoencoders for unsupervised real-time bridge health assessment, Comput.-Aided Civ. Infrastruct. Eng. 38 (8) (2023) 959–974.
[38] Marco Martino Rosso, Angelo Aloisio, Giansalvo Cirrincione, Giuseppe Carlo Marano, Subspace features and statistical indicators for neural network-based damage detection, in: Structures, vol. 56, Elsevier, 2023, 104792.
[39] Dawei Liu, Yuequan Bao, Hui Li, Machine learning-based stochastic subspace identification method for structural modal parameters, Eng. Struct. 274 (2023) 115178.
[40] Hak Bo Shim, Hyo Seon Park, et al., SSI-LSTM network for adaptive operational modal analysis of building structures, Mech. Syst. Signal Process. 195 (2023) 110306.
[41] Dawei Liu, Zhiyi Tang, Yuequan Bao, Hui Li, Machine-learning-based methods for output-only structural modal identification, Struct. Control Health Monit. 28 (12) (2021) e2843.
[42] Jiangpeng Shu, Congguang Zhang, Yifan Gao, Yanbo Niu, A multi-task learning-based automatic blind identification procedure for operational modal analysis, Mech. Syst. Signal Process. 187 (2023) 109959.
[43] Maria Giovanna Masciotta, Daniele Pellegrini, Tracking the variation of complex mode shapes for damage quantification and localization in structural systems, Mech. Syst. Signal Process. 169 (2022) 108731.
[44] Carlo Rainieri, Perspectives of second-order blind identification for operational modal analysis of civil structures, Shock Vib. 2014 (2014).
[45] Wei Guan, L.L. Dong, J.M. Zhou, Yi Han, J. Zhou, Data-driven methods for operational modal parameters identification: A comparison and application, Measurement 132 (2019) 238–251.
[46] Fabien Poncelet, Gaëtan Kerschen, J.C. Golinval, Damien Verhelst, Output-only modal analysis using blind source separation techniques, Mech. Syst. Signal Process. 21 (6) (2007) 2335–2358.
[47] S.I. McNeill, An analytic formulation for blind modal identification, J. Vib. Control 18 (14) (2012) 2111–2121.
[48] Scot McNeill, A modal identification algorithm combining blind source separation and state space realization, J. Signal Inf. Process. 4 (2013) 173–185.
[49] Lieven De Lathauwer, Joséphine Castaing, Blind identification of underdetermined mixtures by simultaneous matrix diagonalization, IEEE Trans. Signal Process. 56 (3) (2008) 1096–1105.
[50] Michael Feldman, Hilbert transform in vibration analysis, Mech. Syst. Signal Process. 25 (3) (2011) 735–802.
[51] Adel Belouchrani, Karim Abed-Meraim, J.F. Cardoso, Eric Moulines, A blind source separation technique using second-order statistics, IEEE Trans. Signal Process. 45 (2) (1997) 434–444.
[52] Wenliang Zhou, David Chelidze, Blind source separation based vibration mode identification, Mech. Syst. Signal Process. 21 (8) (2007) 3072–3087.
[53] Jérôme Antoni, S. Chauhan, A study and extension of second-order blind source separation to operational modal analysis, J. Sound Vib. 332 (4) (2013) 1079–1106.
[54] Jerome Antoni, Roberto Castiglione, Luigi Garibaldi, Interpretation and generalization of complexity pursuit for the blind separation of modal contributions, Mech. Syst. Signal Process. 85 (2017) 773–788.
[55] Petr Tichavsky, Arie Yeredor, Fast approximate joint diagonalization incorporating weight matrices, IEEE Trans. Signal Process. 57 (3) (2008) 878–891.
[56] Hugo Tessier, Vincent Gripon, Mathieu Léonardon, Matthieu Arzel, Thomas Hannagan, David Bertrand, Rethinking weight decay for efficient neural network pruning, J. Imaging 8 (3) (2022) 64.

[57] Changyou Chen, David Carlson, Zhe Gan, Chunyuan Li, Lawrence Carin, Bridging the gap between stochastic gradient MCMC and stochastic optimization, in: Artificial Intelligence and Statistics, PMLR, 2016, pp. 1051–1060.
[58] Yoshua Bengio, Practical recommendations for gradient-based training of deep architectures, in: Neural Networks: Tricks of the Trade: Second Edition, 2012, pp. 437–478.
[59] Prasenjit Mohanty, Daniel J. Rixen, A modified Ibrahim time domain algorithm for operational modal analysis including harmonic excitation, J. Sound Vib. 275 (1–2) (2004) 375–390.
[60] Samir R. Ibrahim, Double least squares approach for use in structural modal identification, AIAA J. 24 (3) (1986) 499–503.
[61] R. Brincker, C. Ventura, Introduction to Operational Modal Analysis, Wiley, 2015.
[62] Richard S. Pappa, Kenny B. Elliott, Axel Schenk, Consistent-mode indicator for the eigensystem realization algorithm, J. Guid. Control Dyn. 16 (5) (1993) 852–858.
[63] Enrique García-Macías, Antonello Ruccolo, Mariano Angelo Zanini, Carlo Pellegrino, Carmelo Gentile, Filippo Ubertini, Paolo Mannella, P3P: A software suite for autonomous SHM of bridge networks, J. Civ. Struct. Health Monit. (2022) 1–18.
[64] Filippo Ubertini, A Luigi Materazzi, Carmelo Gentile, Fabio Pelliccia, et al., Automatic identification of modal parameters: Application to a reinforced concrete arch bridge, in: Proceedings of the EACS, 2012.